Inorganic Chemistry
Article
pubs.acs.org/IC

Paramagnetic One-Dimensional Chains Comprised of Trinuclear Pt–Cu–Pt and Paddlewheel Dirhodium Complexes with Metal–Metal Bonds

Kazuhiro Uemura* and Masahiro Ebihara

Department of Chemistry, Faculty of Engineering, Gifu University, Yanagido 1-1, Gifu, 501-1193, Japan

Ⓢ *Supporting Information*

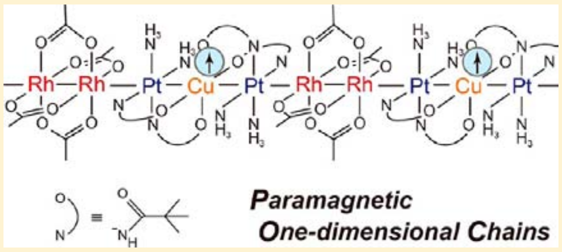

ABSTRACT: One-dimensional (1-D) chain complexes constructed by metal–metal bonds containing three types of metal species—platinum, rhodium, and copper—have been rationally synthesized and characterized by single-crystal X-ray analyses and physical measurements. The paddlewheel or lantern type complex, $[Rh_2(O_2CCH_3)_4]$ (i.e., $[Rh_2]$), has a vacant σ^* orbital which accepts the electrons from the filled d_{z^2} orbital of *cis*-$[Pt(piam)_2(NH_3)_2]\cdot 2H_2O$ (**1**, i.e. [Pt], where piam = pivalamidate) to afford a tetranuclear complex, $[\{Rh_2(O_2CCH_3)_4\}\{Pt(piam)_2(NH_3)_2\}_2]\cdot 2H_2O$ (**2**). Compound **2** forms a linear alignment as $[Pt]-[Rh_2]-[Pt]$ with unbridged Rh–Pt bonds, where the oxygen atoms of the piam ligands in the [Pt] are noncoordinated, showing the capability of binding another metal ion. Simply mixing $[Rh_2]$ and the heterometallic trinuclear complex $[Pt_2Cu(piam)_4(NH_3)_4](PF_6)_2$ (**3**, i.e. [Pt–Cu–Pt]) in a ratio of 1:1 in MeOH, EtOH, or Me_2CO affords $[\{Rh_2(O_2CCH_3)_4\}\{Pt_2Cu(piam)_4(NH_3)_4\}]_n(PF_6)_{2n}$ (**4**), $[\{Rh_2(O_2CCH_3)_4\}\{Pt_2Cu(piam)_4(NH_3)_4\}]_n(PF_6)_{2n}$ (**5**), or $[\{Rh_2(O_2CCH_3)_4\}\{Pt_2Cu(piam)_4(NH_3)_4\}]_n(PF_6)_{2n}\cdot 6nMe_2CO$ (**6**), respectively. Compounds **4**–**6** form infinite chains with the repetition of $-\{[Rh_2]-[Pt-Cu-Pt]\}_n-$, which to our knowledge, are the first examples of heterometallic 1-D chains comprised of three types of metal species with direct metal–metal bonds. The $CF_3CO_2^-$, ClO_4^-, and water molecules influence the crystal packing to form an octanuclear complex of $[\{Rh_2(O_2CCH_3)_4\}\{Pt_2Cu(piam)_4(NH_3)_4\}_2](CF_3CO_2)_2(ClO_4)_2\cdot 2H_2O$ (**7**) with [Pt–Cu–Pt]–[Rh₂]–[Pt–Cu–Pt] alignment. Considering the crystal structures and X-ray photoelectron spectra (XPS) measurements in **4**–**7**, the oxidation states of the metal atoms are $-\{[Rh_2^{II,II}]-[Pt^{II}-Cu^{II}-Pt^{II}]\}_n-$ or $[Pt^{II}-Cu^{II}-Pt^{II}]-[Rh_2^{II,II}]-[Pt^{II}-Cu^{II}-Pt^{II}]$, which are unchanged from those in the starting compounds. Electron paramagnetic resonance spectra of **4**–**7** show axially symmetric spectra with $g_{\parallel} > g_{\perp}$, indicating that the HOMO (SOMO) is a Cu $d_{x^2-y^2}$ orbital. In **7**, the hyperfine coupling in the spectrum indicates that the unpaired spin on Cu is perturbed by the Pt atoms.

■ INTRODUCTION

One-dimensional (1-D) metal complexes have intrigued researchers over the past several decades because of their unusual electrical properties,[1] including progressive resonance Raman spectra, large third-order nonlinear optical properties, and so on.[1d] These 1-D metal complexes are classified into two types of compounds: finite[2,3] and infinite[4,5] compounds. Finite 1-D metal complexes, namely, extended metal atom chains, take advantage of designed organic ligands to align various metals.[3] By varying the length of the ligands, such as polypyridylamidate[3a,g,h] or π conjugated[3c] ligands, the number of aligned metals is exactly regulated, toward advanced materials for single nanolength chains.[3g] In contrast, for infinite 1-D metal complexes, several compounds consisting of –M–M– bonds[4] and a large number of halogen-bridged –M–X– or –M–M–X– chains[5] have been synthesized and investigated. The synthetic approach for infinite chains depends on the metal oxidation states; half-filled (d^7) and filled (d^8) d_{z^2} orbitals are superimposed to form σ bonds and are infinitely crystallized. Therefore, most infinite 1-D metal complexes have made use of $Rh^{+/2+}$,[4a−d,f] $Pd^{2+/3+}$,[4i] and/or $Pt^{2+/3+}$,[4e,g,h] where partial oxidation or reduction of the d_{z^2} orbitals attributed to the $d^7 \leftrightarrow d^8$ redox changes are utilized. Thus, the metal species in infinite 1-D metal complexes are very restricted, giving the expectation of a new approach for the construction using various metal species.

Heterometallic cluster complexes containing direct M–M′ interactions are expected for the multimetallic catalysis and functional materials based on their versatile chemical and physical properties.[6] To obtain the heterometallic cluster complexes containing direct M–M′ interactions, it is effective to utilize Pt→M′ dative bonds, where the d_{z^2} orbital of the square-planar Pt^{2+} center donates electron density to the Lewis-acidic metal, as generally found in Pt–Cu or Pt–Ag compounds with ligand-unsupported $d-d^{10}$ contacts.[6a,c,g,h] Also, with the support of bridging ligands, other metals (M′ = Cu^{2+}, Fe^{3+}, Rh^{3+}, Pd^{2+}, etc.) can closely contact Pt^{2+} ions to afford dinuclear Pt–M′ and trinuclear Pt–M′–Pt complexes,[7−9] where the filled d_{z^2} orbital of Pt^{2+} interacts with M′

Received: February 22, 2013
Published: April 25, 2013

dx.doi.org/10.1021/ic400470g | *Inorg. Chem.* 2013, 52, 5535−5550

Scheme 1

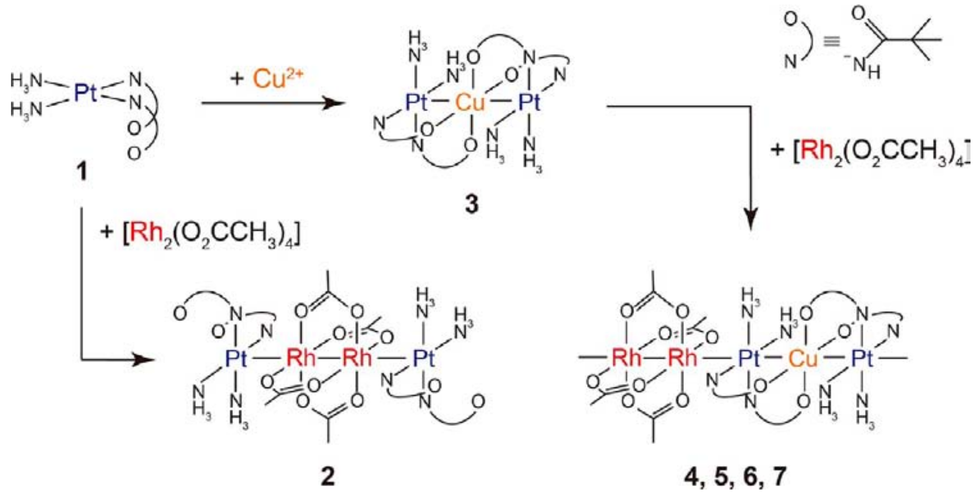

in a face-to-face fashion. The axial Pt^{2+} atoms act as weak σ-donors toward the M′ d orbitals, behaving, in fact, in a manner very similar to a typical ligand.[8d,10] Those Pt−M′ interactions have been utilized in infinite architectures; for example, $[\{Pt(ppy)_2\}_2\{Ag(Me_2CO)\}_2]_n(ClO_4)_{2n}\cdot nMe_2CO$ (Hppy = 2-phenylpyridine) shows a helical chain consisting of an alternating stack of $[Pt(ppy)_2]$ and $[Ag(Me_2CO)]$ units connected by a Pt→Ag dative bond.[6g]

On the basis of this background, we have tried to obtain infinite 1-D metal complexes utilizing the Pt−M′ interaction, to explore characteristic properties in heterometallic chains.[11] Previously, we reported the 1-D chain complex, $[\{Rh_2(O_2CCH_3)_4\}\{Pt_2(piam)_2(NH_3)_4\}_2]_n(PF_6)_{4n}\cdot 6nH_2O$ (where piam = pivalamidate), comprising two types of dinuclear complexes to align $-\{[Pt_2]-[Rh_2]-[Pt_2]\}_n-$, where $[Rh_2]$ is $[Rh_2(O_2CCH_3)_4]$ and $[Pt_2]$ is a pivalamidate-bridged Pt complex.[11d] This compound is rationally constructed with unbridged Rh−Pt bonds between $[Rh_2]$ and $[Pt_2]$, where the highest occupied molecular orbital (HOMO)−lowest unoccupied molecular orbital (LUMO) interaction between the vacant σ^* in $[Rh_2^{II,II}]$ (d^7, d^7) and the filled σ^* in $[Pt_2^{II,II}]$ (d^8, d^8) effectively forms, with the support of quadruple hydrogen bonds between oxygen atoms of carboxylate ligands in $[Rh_2]$ and nitrogen atoms of amine/amidate ligands in $[Pt_2]$. Interestingly, the bridging ligands of $[Rh_2]$ can be changed from acetate to trifluoroacetate of $[\{Rh_2(O_2CCF_3)_4\}\{Pt_2(piam)_2(NH_3)_4\}_2]_n(CF_3CO_2)_{4n}\cdot 2nEtOH\cdot 2nH_2O$ or acetamidate groups of $[\{Rh_2(acam)_4\}\{Pt_2(piam)_2(NH_3)_4\}_2]_n(CF_3CO_2)_{4n}$ (where acam = acetamidate),[11d] indicating the possibility of numerous analogues. Furthermore, by varying the coligands in $[Pt_2]$ with NH_2CH_3 or 2,2′-bipyridine (bpy), hexanuclear 1-D metal complexes of $[\{Rh_2(O_2CCH_3)_4\}\{Pt_2(piam)_2(NH_2CH_3)_4\}_2](PF_6)_4$ and $[\{Rh_2(O_2CCH_3)_4\}\{Pt_2(piam)_2(bpy)_2\}_2](PF_6)_4$ with unbridged Rh−Pt bonds have also been obtained.[11e]

All of the compounds mentioned above are diamagnetic, so we have attempted, as the next challenge, to construct paramagnetic 1-D chain complexes to study the behavior of the unpaired spin in these unique heterometallic chains. Although the generally accepted procedure to obtain paramagnetic 1-D chains is partial oxidization by chemical doping, our strategy is the regular insertion of "third" paramagnetic metals, such as the Cu^{2+} ion. Focusing on amidate-hanging Pt mononuclear complexes cis-$[Pt(piam)_2(NH_3)_2]\cdot 2H_2O$ (**1**),[12] which can easily bind another metal ion with the noncoordinated oxygen atoms in the amide moieties to afford various dinuclear Pt−M′ and trinuclear Pt−M′−Pt complexes, we began with an investigation of the affinity between $[Rh_2]$ and mononuclear **1**. Then, featuring Pt→Rh and Pt→Cu bonds, we set out to access compounds containing both interactions to obtain multinuclear complexes. In this contribution, we first report the syntheses and solid-state characterization of a series of paramagnetic 1-D chain complexes with three defferent metal species, Rh, Pt, and Cu, containing metal−metal bonds (Scheme 1). We also present a study of oxidation states and unpaired spin behaviors by X-ray photoelectron spectroscopy (XPS), electron paramagnetic resonance (EPR) spectroscopy, and density functional theory (DFT) calculations, discussing the electronic structures.

■ EXPERIMENTAL SECTION

Materials. Rhodium(III) chloride trihydrate and potassium tetrachloroplatinate(II) were obtained from Tanaka Kikinzoku Co. Sodium hexafluorophosphate and tetrabutylammonium perchlorate were obtained from Tokyo Chemical Industry Co. $CuCl_2\cdot 2H_2O$ was obtained from Wako Co. cis-$[Pt(piam)_2(NH_3)_2]\cdot 2H_2O$[12] and $[Rh_2(O_2CCH_3)_4]$[13] were synthesized according to the previous procedures.

Synthesis of $[\{Rh_2(O_2CCH_3)_4\}\{Pt(piam)_2(NH_3)_2\}_2]\cdot 2H_2O$ (2). A THF solution (30 mL) of $[Rh_2(O_2CCH_3)_4]$ (0.40 g, 0.09 mmol) was stirred with cis-$[Pt(piam)_2(NH_3)_2]\cdot 2H_2O$ (0.77 g, 0.17 mmol) for 20 min, and the resulted solutions were slowly evaporated. After one week, brown crystals of **2** with a metallic luster were obtained (61 mg). Yield 55%. For elemental analysis, the dehydrated sample was obtained by vacuum drying at room temperature for 24 h. Elemental analysis calcd for $C_{28}H_{64}N_8O_{12}Pt_2Rh_2$: C, 25.85; H, 4.96; N, 8.61%. Found: C, 25.53; H, 4.82; N, 8.30%.

Synthesis of $[Pt_2Cu(piam)_4(NH_3)_4](PF_6)_2$ (3). An aqueous solution (10 mL) of $CuCl_2\cdot 2H_2O$ (85 mg, 0.50 mmol) and $NaPF_6$ (0.34 g, 2.0 mmol) was stirred for several minutes and mixed with a MeOH solution (10 mL) of cis-$[Pt(piam)_2(NH_3)_2]\cdot 2H_2O$ (0.22 g, 0.46 mmol) at room temperature. After two days, light green powders of $[Pt_2Cu(piam)_4(NH_3)_4](PF_6)_2$ were collected by filtration and washed with small amounts of water and dried (0.21 g). Yield: 76%. Elemental analysis calcd for $C_{20}H_{52}CuF_{12}N_8O_4P_2Pt_2$: C, 19.81; H, 4.32; N, 9.24%. Found: C, 19.83; H, 4.05; N, 9.25%.

Synthesis of $[\{Rh_2(O_2CCH_3)_4\}\{Pt_2Cu(piam)_4(NH_3)_4\}]_n(PF_6)_{2n}$ (4). $[Rh_2(O_2CCH_3)_4]$ (12 mg, 0.03 mmol) was added to an EtOH solution (9 mL) of **3** (33 mg, 0.03 mmol) and stirred at room

Table 1. Crystallographic Data and Structure Refinements for $[\{Rh_2(O_2CCH_3)_4\}\{Pt(piam)_2(NH_3)_2\}_2]\cdot 2H_2O$ (2), $[Pt_2Cu(piam)_4(NH_3)_4](PF_6)_2$ (3), $[\{Rh_2(O_2CCH_3)_4\}\{Pt_2Cu(piam)_4(NH_3)_4\}]_n(PF_6)_{2n}$ (4), $[\{Rh_2(O_2CCH_3)_4\}\{Pt_2Cu(piam)_4(NH_3)_4\}]_n(PF_6)_{2n}$ (5), $[\{Rh_2(O_2CCH_3)_4\}\{Pt_2Cu(piam)_4(NH_3)_4\}]_n(PF_6)_{2n}\cdot 6n Me_2CO$ (6), and $[\{Rh_2(O_2CCH_3)_4\}\{Pt_2Cu(piam)_4(NH_3)_4\}_2](CF_3CO_2)_2(ClO_4)_2\cdot 2H_2O$ (7)

	2	3	4
empirical formula	$C_{28}H_{64}N_8O_{14}Pt_2Rh_2$	$C_{20}H_{52}CuF_{12}N_8O_4P_2Pt_2$	$C_{28}H_{64}CuF_{12}N_8O_{12}P_2Pt_2Rh_2$
fw	1332.87	1212.36	1654.35
cryst syst	monoclinic	monoclinic	triclinic
space group	$P2_1/c$	$P2_1/n$	$P\bar{1}$
a (Å)	11.440(2)	10.749(3)	11.259(5)
b (Å)	14.006(3)	16.038(4)	11.690(6)
c (Å)	15.151(3)	12.657(3)	12.126(6)
α (deg)	90	90	113.200(4)
β (deg)	108.771(2)	108.939(3)	99.391(2)
γ (deg)	90	90	108.533(4)
V (Å^3)	2298.5(8)	2063.7(8)	1312.5(11)
Z	2	2	1
temp (K)	293	293	123
D_c (Mgm^{-3})	1.926	1.951	2.093
abs coeff (mm^{-1})	6.835	7.440	6.484
$F(000)$	1292	1166	797
cryst size (mm^3)	0.21 × 0.20 × 0.17	0.09 × 0.09 × 0.09	0.30 × 0.30 × 0.15
measured reflns	18075	16809	10281
independent reflns	5243 [R_{int} = 0.0347]	4726 [R_{int} = 0.0581]	5903 [R_{int} = 0.0394]
data/restraints/params	5243/0/249	4726/67/231	5903/0/314
goodness-of fit on F^2	1.083	1.032	1.032
R [$I > 2\sigma(I)$]	R_1 = 0.0461, wR_2 = 0.1039	R_1 = 0.0631, wR_2 = 0.1452	R_1 = 0.0601, wR_2 = 0.1496
R (all data)	R_1 = 0.0715, wR_2 = 0.1194	R_1 = 0.1043, wR_2 = 0.1783	R_1 = 0.0657, wR_2 = 0.1542
	5	**6**	**7**
empirical formula	$C_{28}H_{64}CuF_{12}N_8O_{12}P_2Pt_2Rh_2$	$C_{46}H_{100}CuF_{12}N_8O_{18}P_2Pt_2Rh_2$	$C_{52}H_{116}Cl_2Cu_2F_6N_{16}O_{30}Pt_4Rh_2$
fw	1654.35	2002.82	2743.77
cryst syst	monoclinic	monoclinic	monoclinic
space group	$P2_1/n$	$P2_1/n$	$C2/c$
a (Å)	13.1305(15)	13.251(3)	22.916(3)
b (Å)	14.0731(15)	20.825(4)	12.9623(14)
c (Å)	13.8857(16)	14.476(3)	33.225(4)
α (deg)	90	90	90
β (deg)	97.1867(13)	111.288(2)	105.7449(13)
γ (deg)	90	90	90
V (Å^3)	2545.7(5)	3722.1(13)	9498.8(19)
Z	2	2	4
temp (K)	123	123	123
D_c (Mgm^{-3})	2.158	1.787	1.919
abs coeff (mm^{-1})	6.686	4.596	6.787
$F(000)$	1594	1978	5312
cryst size (mm^3)	0.20 × 0.20 × 0.15	0.61 × 0.18 × 0.14	0.40 × 0.25 × 0.20
measured reflns	20427	29529	34100
independent reflns	5831 [R_{int} = 0.0253]	8500 [R_{int} = 0.0298]	10602 [R_{int} = 0.0309]
data/restraints/params	5831/0/314	8500/0/428	10602/0/532
goodness-of fit on F^2	1.059	1.117	1.089
R [$I > 2\sigma(I)$]	R_1 = 0.0249, wR_2 = 0.0522	R_1 = 0.0337, wR_2 = 0.0785	R_1 = 0.0391, wR_2 = 0.0913
R (all data)	R_1 = 0.0261, wR_2 = 0.0530	R_1 = 0.0395, wR_2 = 0.0831	R_1 = 0.0432, wR_2 = 0.0947

temperature. After two days, yellow microcrystals were collected by filtration and recrystallized from MeOH (12 mL). Yield: 27%. Elemental analysis calcd for $C_{28}H_{64}CuF_{12}N_8O_{12}P_2Pt_2Rh_2$: C, 20.33; H, 3.90; N, 6.77%. Found: C, 20.02; H, 3.84; N, 6.53%.

Synthesis of $[\{Rh_2(O_2CCH_3)_4\}\{Pt_2Cu(piam)_4(NH_3)_4\}]_n(PF_6)_{2n}$ (5). $[Rh_2(O_2CCH_3)_4]$ (4.4 mg, 10 μmol) was added to an EtOH solution (10 mL) of **3** (12 mg, 10 μmol) and stirred at 40 °C for 1 h and slowly evaporated. After one month, green crystals of **5** with a metallic luster were obtained (13 mg). Yield: 79%. Elemental analysis calcd for $C_{28}H_{64}CuF_{12}N_8O_{12}P_2Pt_2Rh_2$: C, 20.33; H, 3.90; N, 6.77%. Found: C, 20.19; H, 3.74; N, 6.68%.

Synthesis of $[\{Rh_2(O_2CCH_3)_4\}\{Pt_2Cu(piam)_4(NH_3)_4\}]_n(PF_6)_{2n}\cdot 6n Me_2CO$ (6). $[Rh_2(O_2CCH_3)_4]$ (12 mg, 27 μmol) was added to a Me_2CO solution (9 mL) of **3** (33 mg, 27 μmol) and stirred at room temperature for several minutes. Hexane (27 mL) was gently layered on the resulted solution. After three days, yellow crystals of **6** with a metallic luster was collected by filtration and washed with Me_2CO/hexane (1:3 v/v). For the elemental analysis, the samples were dried in *vacuo* for 2 h (40 mg). Yield: 89%. Elemental analysis calcd for $C_{28}H_{64}CuF_{12}N_8O_{12}P_2Pt_2Rh_2$: C, 20.33; H, 3.90; N, 6.77%. Found: C, 19.94; H, 3.57; N, 6.32%.

Synthesis of $[\{Rh_2(O_2CCH_3)_4\}\{Pt_2Cu(piam)_4(NH_3)_4\}_2](CF_3CO_2)_2(ClO_4)_2\cdot 2H_2O$ (7). An aqueous solution (4 mL) of $CuCl_2\cdot 2H_2O$ (34 mg, 0.20 mmol) and $NaCF_3CO_2$ (0.11 g, 0.81 mmol) was stirred for several minutes and mixed with a Me_2CO solution (4 mL) of *cis*-$[Pt(piam)_2(NH_3)_2]\cdot 2H_2O$ (86 mg, 0.18 mmol) at room temperature and slowly evaporated. After several days, green crystals of $[Pt_2Cu(piam)_4(NH_3)_4](CF_3CO_2)_2\cdot 2Me_2CO$, whose crystal structure was confirmed by single-crystal X-ray analyses, were collected by filtration and dried (77 mg). An EtOH solution (7 mL) of $[Pt_2Cu(piam)_4(NH_3)_4](CF_3CO_2)_2$ (23 mg, 0.02 mmol) was mixed with $[Rh_2(O_2CCH_3)_4]$ (4.4 mg, 0.01 mmol) and Bu_4NClO_4 (6.8 mg, 0.02 mmol) and stirred at room temperature and slowly evaporated at 30 °C. After several days, green crystals of **7** were obtained by filtration and dried (13 mg). Yield: 45%. Elemental analysis calcd for $C_{52}H_{120}Cl_2Cu_2F_6N_{16}O_{30}Pt_4Rh_2$: C, 22.73; H, 4.40; N, 8.16%. Found: C, 22.81; H, 4.28; N, 8.08%.

X-Ray Structure Determination. Measurements were carried out on a Rigaku AFC7R Mercury CCD diffractometer equipped with a normal focus Mo-target X-ray tube (λ = 0.71070 Å) operated at 15 kW power (50 kV, 300 mA) and a CCD two-dimensional detector. A total of 744 frames were collected with a scan width of 0.5° with an exposure time of 5 (**2**), 25 (**3**), 5 (**4**), 3 (**5**), 5 (**6**), and 5 (**7**) s/frame. Empirical absorption correction[14] was performed for all data. The structures were solved by the direct method[15] with the subsequent difference Fourier syntheses and the refinement with the SHELX-97[16] operated by Yadokari-XG software package.[17] Non-hydrogen atoms were refined anisotropically, and all hydrogen atoms were treated as riding atoms. In **2** and **7**, the oxygen atoms of water molecules were refined without hydrogen atoms. The crystal data and structure refinement results are summarized in Table 1.

Physical Measurements. The XPS measurements were carried out on a Quantera-SXM spectrometer at room temperature. Binding energies were measured relative to the C 1s peak (284.8 eV) of internal hydrocarbon. The diffuse reflectance spectra were recorded on a Hitachi U-4000 spectrophotometer over the range from 200 to 2500 nm at room temperature. Obtained reflectance spectra were converted to absorption spectra using the Kubelka–Munk function $F(R_\infty)$. The IR spectra were recorded on a Perkin-Elmer Spectrum 400 over the range from 400 to 2000 cm^{-1} at room temperature. EPR spectra were measured on a JEOL TE-200 spectrometer. Field sweep was monitored with an Echo Electronics EFM-2000 ^1H NMR gaussmeter, the probe of which was attached beside the EPR cavity. The field difference between the EPR and NMR sample positions was calibrated by measuring the field intensity at the resonance of DPPH (g = 2.00354).

DFT Calculation. The electronic structures of model compounds $[\{Rh_2(O_2CCH_3)_4\}\{Pt(NHCOCH_3)_2(NH_3)_2\}_2]$ and $[\{Rh_2(O_2CCF_3)_4\}\{Pt(NHCOCH_3)_2(NH_3)_2\}_2]$ were calculated with the DFT method using the B3LYP functional[18] with the Gaussian 09 program package.[19] For Pt and Rh, the LANL2DZ basis set was used together with the effective core potential of Hay and Wadt.[20] For the other elements, the 6-31G* basis sets[21] were selected. The models of $[\{Rh_2(O_2CCH_3)_4\}\{Pt(NHCOCH_3)_2(NH_3)_2\}_2]$ and $[\{Rh_2(O_2CCF_3)_4\}\{Pt(NHCOCH_3)_2(NH_3)_2\}_2]$ were generated by using the geometrical parameters obtained from crystal structure data of **2**. For both models, full geometry optimizations were carried out, and on the basis of the structures, 40 singlet excited states were obtained to determine the vertical excitation energies using the time-dependent (TD) DFT calculations.[22]

RESULTS AND DISCUSSION

UV–Vis Spectra on Titrating $[Rh_2(O_2CCH_3)_4]$ with 1. Interaction of $[Rh_2(O_2CCH_3)_4]$ (= $[Rh_2]$) with **1** in solution was confirmed by UV–vis spectroscopy of solutions containing both $[Rh_2]$ and **1**. Figure 1 shows the UV–vis spectra of THF solutions containing $[Rh_2]$ (0.5 mM) and various amounts of **1** in the ratio of 1:n (n = 0, 1, 2, ..., 10). The spectrum of $[Rh_2]$ (n = 0) exhibits two bands at 444 and 597 nm attributed to $\pi^*(Rh_2) \rightarrow \sigma^*(Rh{-}O)$ and $\pi^*(Rh_2) \rightarrow \sigma^*(Rh_2)$ transitions,[23] respectively. In addition to the original two bands of $[Rh_2]$, three new bands at 327, 651, and around 830 nm grow as the concentration of **1** increases, which indicates that $[Rh_2]$ interacts with **1** to afford new species. Although we attribute the new bands to the formation of the crystallographically characterized 1:2 adduct, the monotonic increase in peak intensities above 2 equiv suggests that several equilibria with a different stoichiometry are involved in this system. The THF solution of $[Rh_2]$ and **1** in the ratio of 1:10 is slowly concentrated in the air, resulting in the precipitation of brown microcrystals. By single-crystal X-ray analysis, the cell parameters of the deposited brown crystals are similar to those found in $[\{Rh_2(O_2CCH_3)_4\}\{Pt(piam)_2(NH_3)_2\}_2]\cdot 2H_2O$ (**2**).

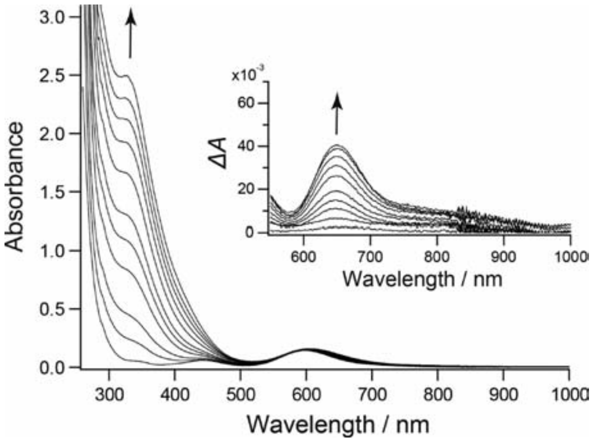

Figure 1. UV–vis spectra of 0.5 mM solution of $[Rh_2(O_2CCH_3)_4]$ in THF containing 0 to 10 equiv of *cis*-$[Pt(piam)_2(NH_3)_2]\cdot 2H_2O$ (**1**) at room temperature. Inset: Each difference spectrum from 0.5 mM solution of $[Rh_2(O_2CCH_3)_4]$.

Crystal Structure of $[\{Rh_2(O_2CCH_3)_4\}\{Pt(piam)_2(NH_3)_2\}_2]\cdot 2H_2O$ (2). Figure 2 shows the crystal structure of **2** measured at 293 K. The paddlewheel dinuclear complex of $[Rh_2(O_2CCH_3)_4]$ is sandwiched by *cis*-$[Pt(piam)_2(NH_3)_2]$ (= [Pt]) at both ends with metal–metal bonds to form tetranuclear $[Pt]{-}[Rh_2]{-}[Pt]$ units, where a crystallographic inversion center lies at the center of the Rh complex (Figure 2a). The Pt mononuclear complexes are bonded to a Rh complex with a bond distance of Rh(1)–Pt(1) = 2.8208(8) Å and a torsion angle O–Rh–Pt–N of about 30° (Figure 2b). Between $[Rh_2]$ and [Pt], the unbridged Rh–Pt bonds are supported by hydrogen bonds between the carboxylate oxygen atoms in the $[Rh_2]$ and the nitrogen atoms of the amine/amidate ligands in the [Pt] with O–N bond distances of 2.99–3.17 Å. The bite angle (τ) between the Rh and Pt coordination planes is 2.9°, which is caused by the relatively stronger hydrogen bonds from amine to carboxylate ligands (N–O = 2.99, 3.02 Å) than those from piam (N–O = 3.03, 3.17 Å). Dihedral angles between the amide planes of piam and the Pt coordination plane are 57° and 35°. As shown in Figure 2c, both O(1) and O(2) atoms in piam ligands are hydrogen bonded to the amine ligands in neighboring tetranuclear units. Each tetranuclear unit is stacked in a slipped fashion with the Pt···Pt distance of 3.52 Å, showing no metal–metal bonds, where quadruple hydrogen bonds between piam and amine ligands are formed. In addition, hydrogen bonds are formed between the oxygen atoms of the piam ligands and

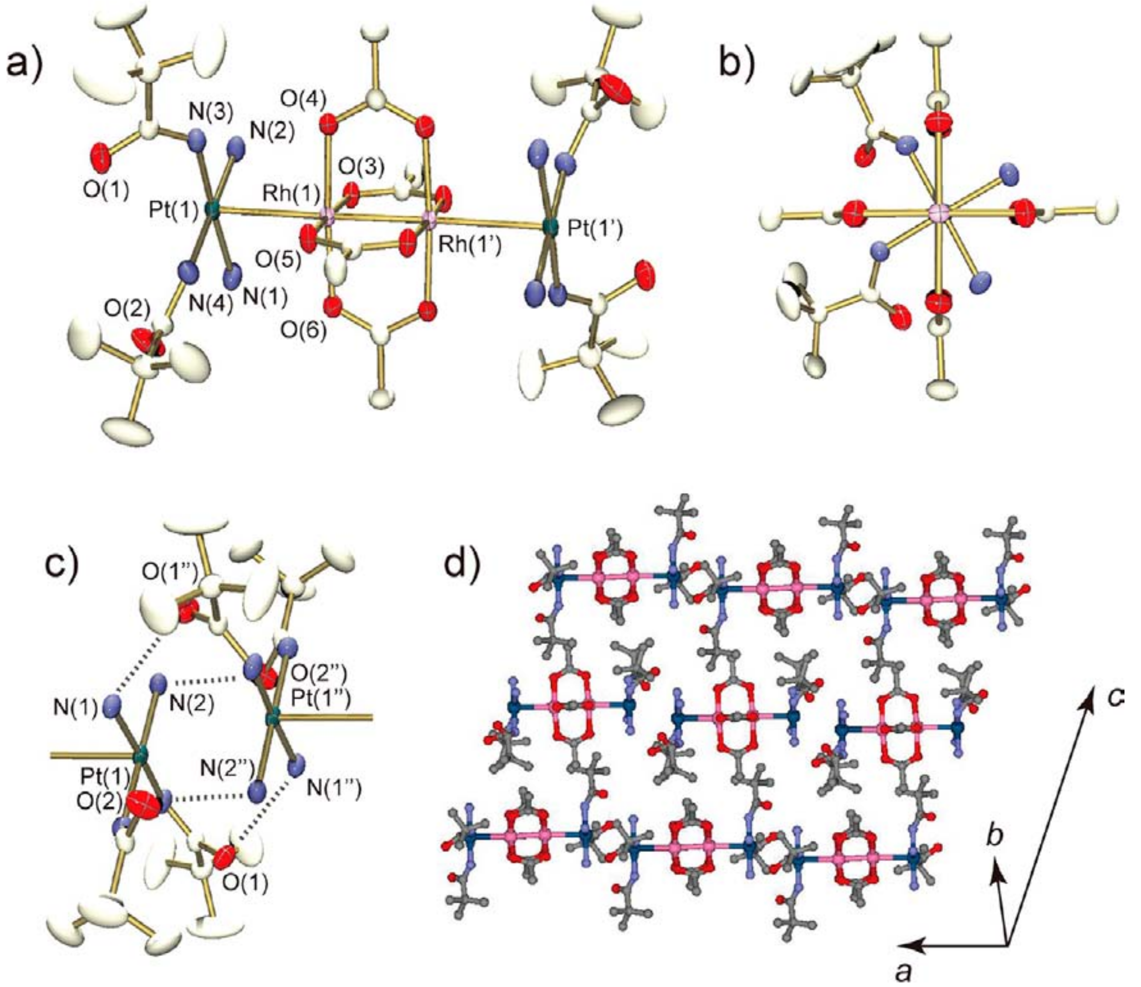

Figure 2. (a) Crystal structure of $[\{Rh_2(O_2CCH_3)_4\}\{Pt(piam)_2(NH_3)_2\}_2]\cdot 2H_2O$ (**2**). (b) Stacking fashion between $[Rh_2]$ and [Pt]. (c) Relationship of two end [Pt] among teteranuclear units with hydrogen bonds indicated as dotted lines. (d) Packing view of tetranuclear units in **2**. The hydrogen atoms and water molecules are omitted for clarity.

accommodated water molecules (Figure S2). In the whole crystal, each tetranuclear $[Pt]-[Rh_2]-[Pt]$ unit is packed in a parallel fashion (Figure 2d). Taking into account that the sum of the metal oxidation numbers of $[Pt]-[Rh_2]-[Pt]$ in **2** is +8, which was obtained from single-crystal X-ray analysis, each oxidation state can be considered as being $[Pt^{II}]-[Rh_2^{II,II}]-[Pt^{II}]$, which is unchanged from that in the starting compounds. The results of the UV−vis spectra and crystal structure show that Pt^{2+} atoms in **1** axially interact with Rh atoms of $[Rh_2(O_2CCH_3)_4]$ through the interaction of the filled d_{z^2} orbital of Pt^{2+} and the vacant $\sigma^*(Rh_2)$ orbital.

The mode of hydrogen bonds between piam, amine, and water molecules changes at lower temperatures, where the crystal system transforms: at 293 K, monoclinic, $a = 11.440(2)$ Å, $b = 14.006(3)$ Å, $c = 15.151(3)$ Å, $\beta = 108.771(2)°$; and at 123 K, triclinic, $a = 11.335(9)$ Å, $b = 13.797(10)$ Å, $c = 15.025(12)$ Å, $\alpha = 90.524(15)°$, $\beta = 109.286(14)°$, $\gamma = 90.491(11)°$. The number of independent atoms measured at 123 K doubles compared with that at 293 K. The most significant difference found in these structures is the Pt−Pt distances between tetranuclear units, which become shorter at lower temperatures: at 293 K, 3.52 Å, and at 123 K, 3.40 and 3.42 Å. Such a transformation is attributed to hydrogen bonds between the tetranuclear units, where the oxygen atom in one piam ligand is strongly hydrogen bonded to an adjacent amine ligand at the *cis* position and accommodated water molecules, resulting in quadruple hydrogen bonds between tetranuclear units at 293 K becoming double hydrogen bonds at 123 K (Figure S2).

Metal Binding Ability of 1 and Crystal Structure of $[Pt_2Cu(piam)_4(NH_3)_4](PF_6)_2$ (3). Compound **1** could be considered as a good precursor of di- or trinulcear complexes with Cu^{2+} ions because it possesses pendant arms of amidate ligands, involving the donation of electron density from the filled d_{z^2} orbital of Pt^{2+} to the Lewis-acidic Cu^{2+} ion.[8g] Figure 3 shows the UV−vis spectra of $CuCl_2\cdot 2H_2O$ (5 mM) in MeOH with the addition of 0 to 3 equiv of **1**. As **1** is added, the peak around 870 nm attributed to the d−d transition in Cu^{2+} ions decreases and a new peak around 660 nm increases, indicating that Cu^{2+} ions are interacting with **1**.[10] The absorbances at 870 nm were plotted against the mole fraction of the two components, showing that this reaction affords a 1:2 adduct.

By simply mixing *cis*-$[Pt(piam)_2(NH_3)_2]\cdot 2H_2O$, $CuCl_2\cdot 2H_2O$, and $NaPF_6$ in $MeOH/H_2O$, free oxygen atoms of the amidate-hanging Pt complex bind Cu ions to afford the heterometallic trinuclear complex, $[Pt_2Cu(piam)_4(NH_3)_4](PF_6)_2$ (= [Pt−Cu−Pt], **3**). Figure 4 shows the crystal structure of **3** at 293 K. The Cu is situated at the inversion center, in which the coordination sphere is completed by the four equatorial oxygen atoms of the piam ligands and the two Pt

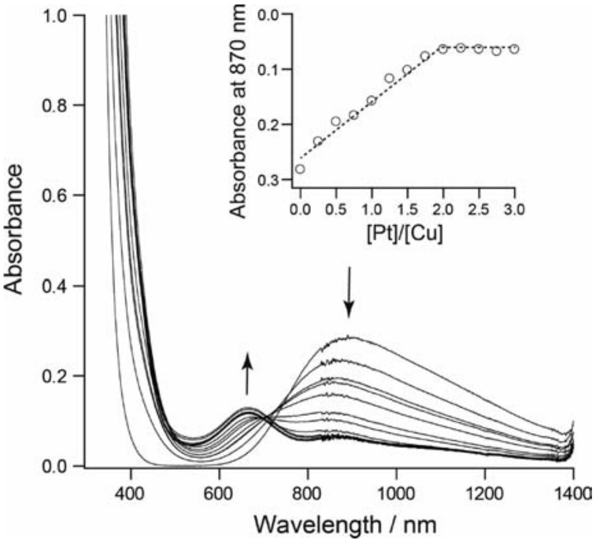

Figure 3. UV−vis spectra of 5 mM solution of $CuCl_2 \cdot 2H_2O$ in MeOH containing 0 to 3 equiv of *cis*-$[Pt(piam)_2(NH_3)_2] \cdot 2H_2O$ (**1**) at room temperature. Inset: Absorbance at 870 nm against the mole fraction of the $CuCl_2 \cdot 2H_2O$ and **1**.

atoms sitting above and below. The Cu atom is sandwiched by two Pt atoms through the four bridging piam ligands, affording a linear Pt−Cu−Pt alignment. The Pt−Cu distance is 2.6870(6) Å, which is similar to the values (2.63−2.98 Å) in other [Pt−Cu−Pt] complexes.[8] The coordination environments of Pt and Cu are eclipsed (Figure 4b). The bite angle between the Pt(1) and Cu(1) coordination planes is 16.6°. The sum of the metal oxidation numbers in [Pt−Cu−Pt] is +6. Taking into account that Pt^{3+} complexes favor being axially coordinated with anions,[23,24] the oxidation state of **3** is $[Pt^{II}-Cu^{II}-Pt^{II}]$. The amine moieties are hydrogen bonded to PF_6^- ions with distances of 3.0−3.1 Å, where PF_6^- ions bridge two trinuclear units. Adjacent trinuclear complexes are related with Pt−Pt separations of 7.87 Å, which is too long to imply any significant interaction (Figure S3). This crystal is also involved with a phase transition depending on temperature: at lower temperature, the crystallinity of **3** collapses. This phase transition is probably attributed to the hydrogen bonds between amine ligands and PF_6^- ions.

Crystal Structures of $[\{Rh_2(O_2CCH_3)_4\}\{Pt_2Cu(piam)_4(NH_3)_4\}]_n(PF_6)_{2n}$ (4), $[\{Rh_2(O_2CCH_3)_4\}\{Pt_2Cu(piam)_4(NH_3)_4\}]_n(PF_6)_{2n}$ (5), and $[\{Rh_2(O_2CCH_3)_4\}\{Pt_2Cu(piam)_4(NH_3)_4\}]_n(PF_6)_{2n} \cdot 6n Me_2CO$ (6). As mentioned above, Pt^{2+} ions in **1** axially interact with both $[Rh_2]$ and Cu^{2+} to afford a ligand-unsupported tetranuclear $[Pt]-[Rh_2]-[Pt]$ complex or a ligand-supported [Pt−Cu−Pt] complex, respectively. The Pt^{2+} ions in **1** interact with both Rh and Cu atoms as bridging ligands, leading to a new class of heterometallic system when both interactions are utilized. As found in the crystal structure of **2** (Figure 2c), the additional metal ions could be incorporated into the terminal sites and housed among each tetranuclear complex.

By simply mixing $[Rh_2]$ and **3** in a ratio of 1:1 in MeOH, EtOH, or Me_2CO, single crystals of $[\{Rh_2(O_2CCH_3)_4\}\{Pt_2Cu(piam)_4(NH_3)_4\}]_n(PF_6)_{2n}$ (**4**), $[\{Rh_2(O_2CCH_3)_4\}\{Pt_2Cu(piam)_4(NH_3)_4\}]_n(PF_6)_{2n}$ (**5**), and $[\{Rh_2(O_2CCH_3)_4\}\{Pt_2Cu(piam)_4(NH_3)_4\}]_n(PF_6)_{2n} \cdot 6n Me_2CO$ (**6**) with metallic luster were obtained. Figures 5−7 show the crystal structures of **4**−**6**, respectively. The most remarkable structural feature in **4**−**6** is that paddlewheel dinuclear complexes of $[Rh_2(O_2CCH_3)_4]$ are linked by $[Pt_2Cu(piam)_4(NH_3)_4]$ units at both ends with metal−metal bonds to give 1-D chains expressed as −[Rh−Rh]−[Pt−Cu−Pt]−, where a crystallographic inversion center is positioned at the center of the Rh complex. To the best of our knowledge, these are the first examples of 1-D chains comprised of metal−metal bonds containing three different metal species, although there are several compounds containing two different transition metals.[6g,11,25,26]

In **4**, the Pt atoms are bonded to a Rh complex with a distance of Pt(1)−Rh(1) = 2.7749(11) Å (Figure 5a) and a typical torsion angle of about 45° (Figure 5b). Multiple hydrogen bonds between nitrogen atoms at amine/amidate ligands coordinated to Pt atoms and carbonyl oxygen atoms in

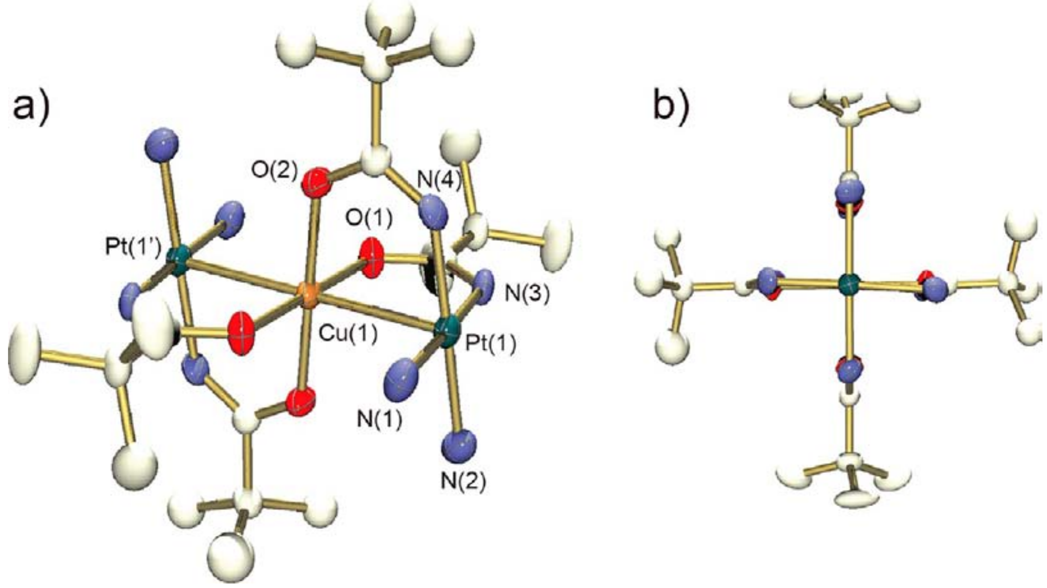

Figure 4. (a) Crystal structure of $[Pt_2Cu(piam)_4(NH_3)_4](PF_6)_2$ (**3**). (b) View along the metal−metal bond in **3**. The hydrogen atoms and PF_6^- ions are omitted for clarity.

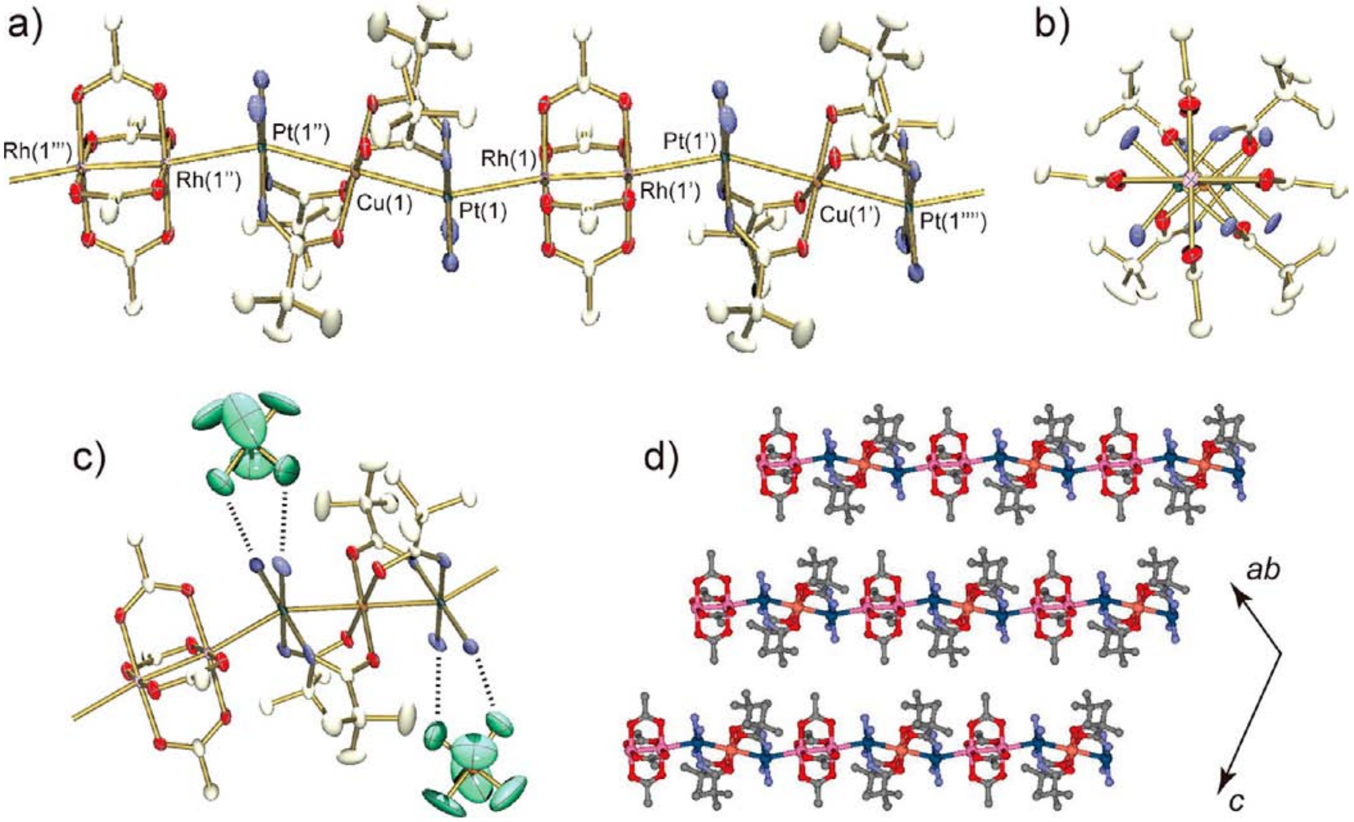

Figure 5. (a) Crystal structure of $[\{Rh_2(O_2CCH_3)_4\}\{Pt_2Cu(piam)_4(NH_3)_4\}]_n(PF_6)_{2n}$ (**4**). (b) View along the metal−metal bond in **4**. (c) Hydrogen bonds between the chain and PF_6^- ions shown as dotted lines. (d) Crystal packing of the 1D chains in **4**. Hydrogen atoms and PF_6^- ions are omitted for clarity.

a Rh complex with distances of 3.02−3.24 Å support these unbridged metal−metal bonds. As shown in Figure 5a, the 1-D backbones of **4** are zigzag chains with a bending angle of Rh(1)−Pt(1)−Cu(1) = 155.010(19)°, rather than Rh(1′)−Rh(1)−Pt(1) = 172.59(5)° and Pt(1)−Cu(1)−Pt(1′) = 180°. Although the bite angle τ between the RhO_4 and PtN_4 planes is small (1.2°), indicating that the Rh and Pt planes are arranged in a face-to-face manner, τ between the PtN_4 and CuO_4 planes is relatively large (19.7°), which is caused by the half-lantern fashion of the piam bridges in the $[Pt_2Cu(piam)_4(NH_3)_4]$ unit. The distance between the Pt and Cu ions is 2.7034(9) Å, which is longer than that in **3** (2.6870(6) Å). The PF_6^- ions are hydrogen bonded to amine ligands coordinated to Pt atoms with distances of 3.13 and 3.16 Å (Figure 5c). As shown in Figure 5d, each zigzag chain is aligned in a parallel fashion in the whole crystal.

Similarly, both **5** and **6** form 1-D chains expressed as −[Rh(1′)−Rh(1)]−[Pt(1)−Cu(1)−Pt(1″)]− (Figures 6 and 7). The most significant difference between **4**−**6** is the linearity, where the angles of Rh(1)−Pt(1)−Cu(1) are 155.010(19)° (**4**), 164.340(7)° (**5**), and 170.711(9)° (**6**), showing that **5** and **6** are moderately zigzag and straight chains, respectively (Figures 6a and 7a). The torsion angles around the coordination axes between the RhO_4 and PtN_4 planes reflect these types of linearity (Figures 5b, 6b, and 7b): 40−43° (**4**), 33−37° (**5**), and 7−9° (**6**), showing that $[Rh_2]$ and [Pt−Cu−Pt] units in zigzag and straight chains are bound roughly in staggered (**4** and **5**) and eclipsed (**6**) fashions. These differences are caused by the crystal-packing effect and solvent molecules accommodated in the crystals. In **6**, Me_2CO molecules are hydrogen bonded to amine ligands with distances of 2.97 and 3.05 Å as well as PF_6^- ions (Figure 7c) affording the single crystals, although their crystallinity is fragile. In contrast, **4** and **5**, which are isomeric with each other, are stable because of the absence of solvent molecules. Taking into account that the density of **5** (2.158 g cm^{-3}) is larger than that of **4** (2.093 g cm^{-3}), compound **5** is more thermodynamically stable.

Crystal Structure of $[\{Rh_2(O_2CCH_3)_4\}\{Pt_2Cu(piam)_4(NH_3)_4\}_2](CF_3CO_2)_2(ClO_4)_2 \cdot 2H_2O$ (7). Interestingly, the crystal structures of these types of 1-D chain depend on the counteranions in the crystals. Figure 8 shows the crystal structure of **7**, containing $CF_3CO_2^-$ and ClO_4^- ions as counteranions. Both anions are more interactive toward the complexes than the PF_6^- ion, showing a different type of structure from **4**−**6**. In **7**, $[Pt_2Cu(piam)_4(NH_3)_4]$ units are axially connected to the paddlewheel dinuclear complex of $[Rh_2(O_2CCH_3)_4]$ at both ends with metal−metal bonds to give an octanuclear complex aligned one-dimensionally as [Pt(2)−Cu(1)−Pt(1)]−[Rh(1)−Rh(1′)]−[Pt(1′)−Cu(1′)−Pt(2′)], where a crystallographic inversion center is positioned at the center of the Rh complex (Figure 8a and b). The $CF_3CO_2^-$ and ClO_4^- ions are hydrogen bonded to amine ligands coordinated to Pt atoms with distances of 2.91−3.04 Å (Figure 8c), where these ions obstruct any further extension. Differently from **4**−**6**, octanuclear complexes are perpendicular to one another in the whole crystal (Figure 8d). As shown in Figure 8b, $[Rh_2]$ and [Pt−Cu−Pt] are stacked with a torsion angle of 19−20°, which is smaller than those of **4** and **5**, and larger than **6**. The angle of

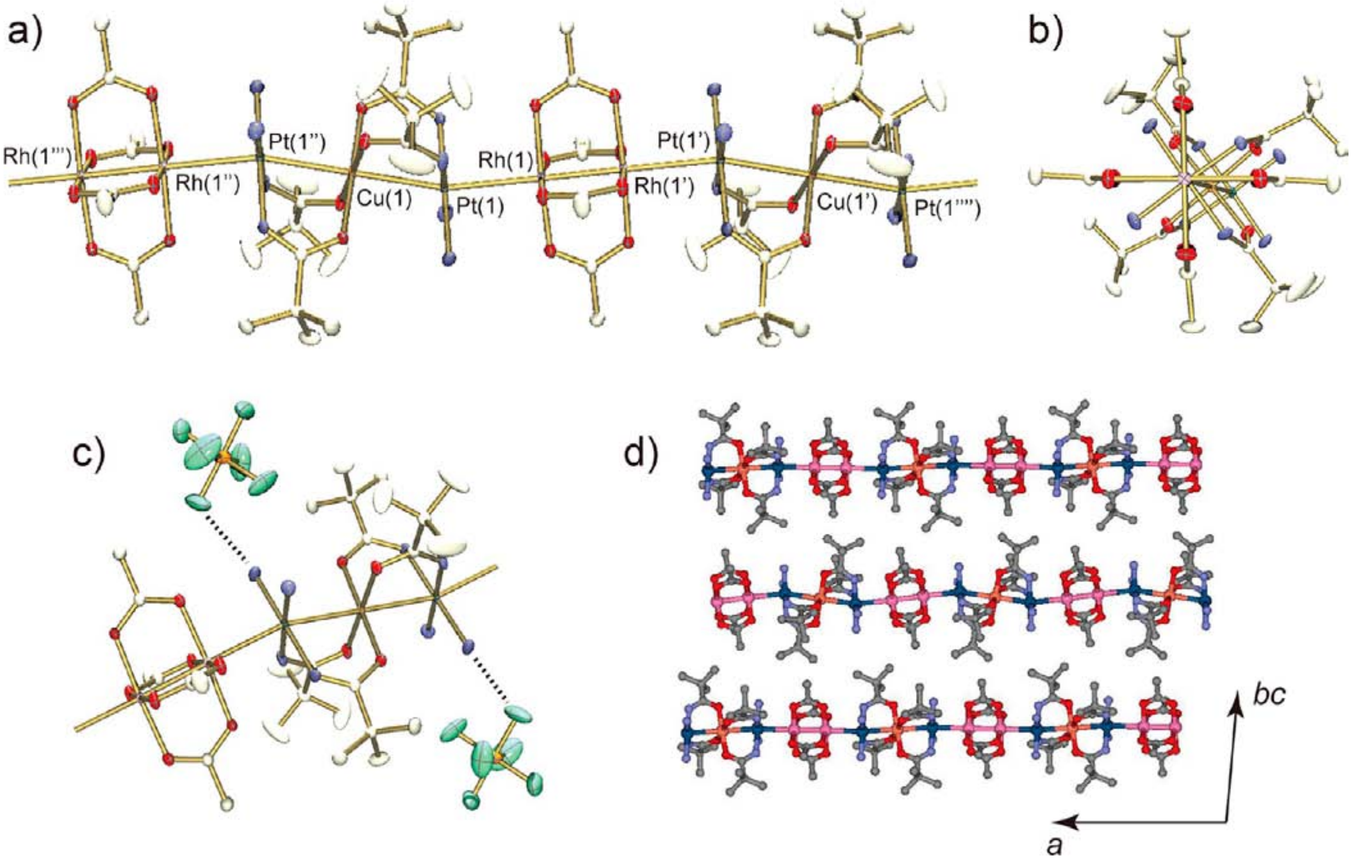

Figure 6. (a) Crystal structure of $[\{Rh_2(O_2CCH_3)_4\}\{Pt_2Cu(piam)_4(NH_3)_4\}]_n(PF_6)_{2n}$ (**5**). (b) View along the metal−metal bond in **5**. (c) Hydrogen bonds between the chain and PF_6^- ions shown as dotted lines. (d) Crystal packing of the 1D chains in **5**. Hydrogen atoms and PF_6^- ions are omitted for clarity.

Rh(1)−Pt(1)−Cu(1) in **7** is also an intermediate value (166.434(19)°) between **5** and **6**.

Comparison of Crystal Structures. Simply mixing $[Rh_2(O_2CCH_3)_4]$ with $[Pt_2Cu(piam)_4(NH_3)_4]^{2+}$ and anions in various solvents affords three types of infinite 1-D chain (**4**−**6**) and a finite 1-D metal complex (**7**). Tables 2 and S2−S5 summarize the metal−metal distances and selected angles for **2**−**7**, defined in Scheme 2. As well as at 123 K, compounds **4**−**7** were also characterized by single-crystal X-ray analyses at 293 K, the results showing no phase transition over the temperature range 123−293 K. The metal−metal distances at 293 K are longer than those at 123 K (Table S2), leading to the thermal expansion of cell volumes. As shown in Table 2, the Rh−Rh distances in **2** and **4**−**7** are 2.37−2.40 Å, which are similar to that in $[Rh_2^{II,II}(O_2CCH_3)_4(H_2O)_2]$ (2.3855(5) Å).[27] In contrast, the Rh−Pt and Pt−Cu distances are 2.77−2.82 Å and 2.65−2.71 Å, respectively, which are more variable. Those variable distances originate from the stacking fashion of $[Rh_2]$ and [Pt−Cu−Pt], where the torsion angle of ϕ_2 around the axis through Rh and Pt coordination planes is an important factor in this system. A smaller ϕ_2 makes the angle θ_2 of Rh−Pt−Cu closer to 180° and the bite angle τ_3 between Pt and Cu coordination planes smaller (Figure 9). As mentioned above, the angle θ_2 of Rh−Pt−Cu dominates the linearity of 1-D backbones, where smaller ϕ_2 values lead to straight chains, although there is no significant relationship between ϕ_2 and Rh−Pt distances. On the other hand, the bite angle τ_3 varies in proportion to the Pt−Cu distance, with the result that smaller ϕ_2 values lead to shorter Pt−Cu distances. Actually, as ϕ_2 values become smaller, the Pt−Cu distances decrease, 2.7034(9) Å (**4**) > 2.6716(3) Å (**5**) > 2.6540(5) Å (**6**); in particular, **6** has an appreciably shorter distance than that (2.6870(6) Å) of the original trinuclear complex **3**. In the octameric structure of **7**, two types of Pt−Cu distances are found, where the inner Pt−Cu distance (2.7094(6) Å) is longer than the outer distances (2.6560(6) Å).

Table 3 summarizes the Rh−Pt distances of **2**−**7** and the related compounds.[11a,c−e,28] In all compounds, bridged and unbridged Rh−Pt distances are shorter than the sum of the van der Waals radii (4.1 Å) of Rh and Pt atoms,[29] indicating overlap of the d_{z^2} orbitals. The metal oxidation states in the previous compounds are $Rh^{II}−Pt^{II}$ or $Rh^{III}−Pt^{II}$ in both bridged and unbridged compounds.[11a,c−e,28] The unbridged Rh−Pt distances in **2**−**7** are longer than the bridged distances[11a,c,28] and also longer than that of the prototype compound $[\{Rh_2(O_2CCH_3)_4\}\{Pt_2(piam)_2(NH_3)_4\}_2]_n(PF_6)_{4n}·6nH_2O$.[11d]

Metal Oxidation States in 4−7. The sum of metal oxidation states for the $[Rh_2]$−[Pt−Cu−Pt] pentameric segments in **4**−**6** are +10, which were determined from the number of PF_6^- ions per pentameric unit in the X-ray structure refinement. In contrast, in **7**, the sum of metal oxidation states of +16 for the octanuclear complex was deduced from the two $CF_3CO_2^-$ and two ClO_4^- ions per octameric segment. Taking into account the similar Rh−Rh distances to $[Rh_2^{II,II}(O_2CCH_3)_4(H_2O)_2]$, it is reasonable that the oxidation states of the Rh parts in **4**−**7** are $[Rh_2^{II,II}]$, resulting in the sum of oxidation states of the [Pt−Cu−Pt] unit being +6.

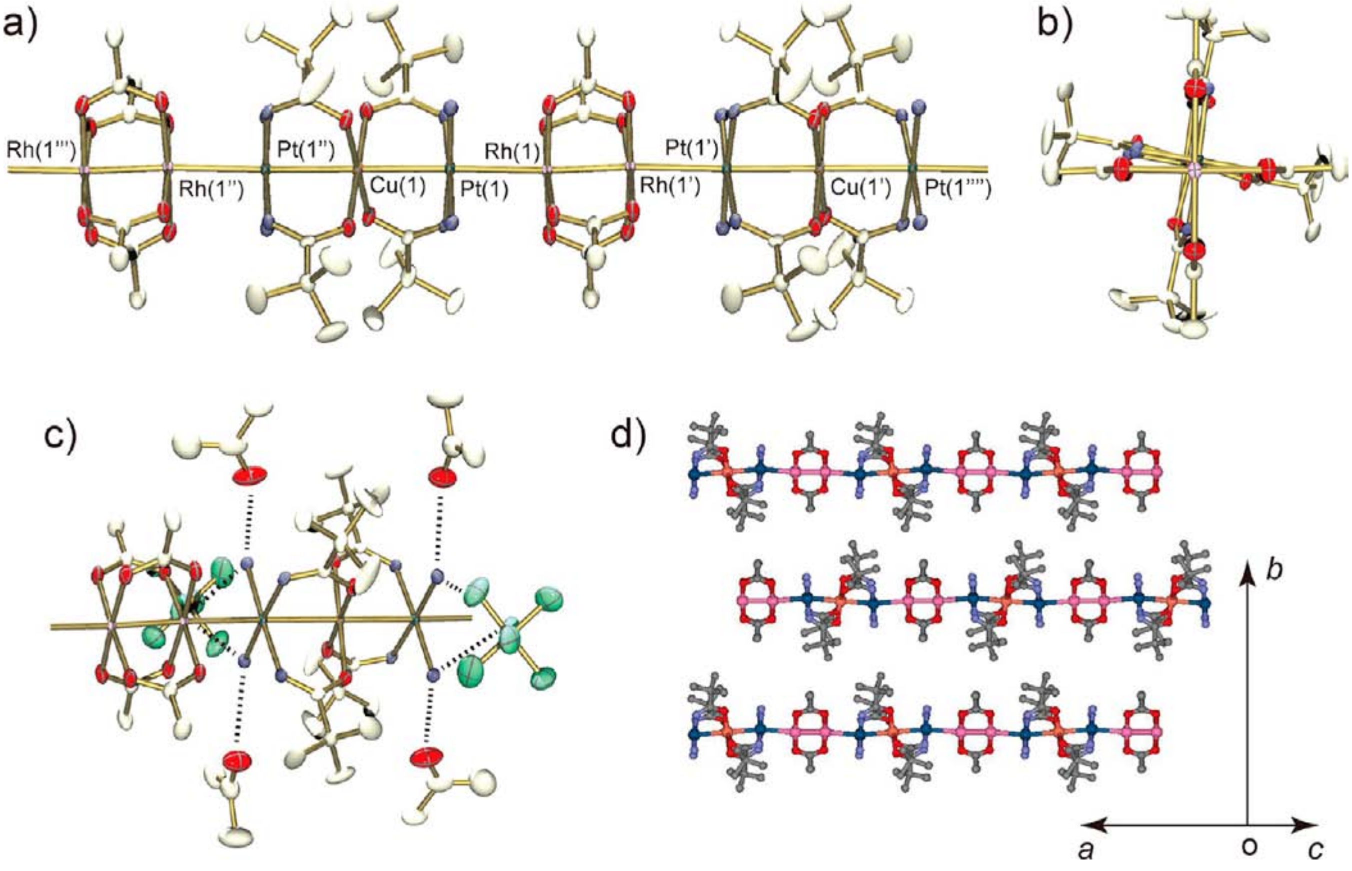

Figure 7. (a) Crystal structure of $[\{Rh_2(O_2CCH_3)_4\}\{Pt_2Cu(piam)_4(NH_3)_4\}]_n(PF_6)_{2n}\cdot 6n Me_2CO$ (**6**). (b) View along the metal−metal bond in **6**. (c) Hydrogen bonds between the chain and PF_6^- ions or Me_2CO shown as dotted lines. (d) Crystal packing of the 1D chains in **6**. Hydrogen atoms, PF_6^- ions, and Me_2CO molecules are omitted for clarity.

To determine further the metal oxidation states in **4**−**7**, XPS measurements were carried out (Figures 10 and S9). The $3d_{3/2}$ signals of Rh are overlapped with the Pt $4d_{5/2}$ signals. The Rh $3d_{5/2}$ binding energies were 308.9 (**2**), 308.9 (**4**), 308.7 (**5**), and 308.8 (**7**) eV, which are close to the value for $[Rh_2^{II,II}(O_2CCH_3)_4]$ (309.0 eV).[30] Figure 10 shows the XPS spectra in the Pt 4f and Cu 2p regions at room temperature, whose binding energies (eV) are summarized in Table 4. The Pt $4f_{7/2}$ binding energies for **1** and **2** were determined as 72.7 and 72.7 eV, respectively, which are closer to that of $[Pt_2^{II,II}(en)_2(\alpha\text{-pyridonato})_2](NO_3)_2$ (73.1 eV; en = ethylenediamine) than to that of $[Pt_2^{III,III}(NH_3)_4(\alpha\text{-pyrrolidonato})_2(NO_3)_2](NO_3)_2$ (74.6 eV).[31] Although the Pt $4f_{7/2}$ binding energy for **3** (73.2 eV), **4** (73.3 eV), **5** (73.2 eV), and **7** (73.0 eV), all of which contain the [Pt−Cu−Pt] unit, are also closer to that of Pt(+2), both Pt $4f_{7/2}$ and $4f_{5/2}$ for **3**−**5** and **7** are shifted to higher energy than those of **1** and **2** (Figure 10, right), which might be caused by charge fluctuation in the Pt atoms. The Cu $2p_{3/2}$ binding energies for **3**, **4**, **5**, and **7** are 932.4, 932.3, 932.2, and 932.2 eV, respectively, with a shoulder. Considering the crystal structure and oxidation state of **3**, it is suggested that the formal oxidation states of **4**−**6** and **7** are $-\{[Rh_2^{II,II}]-[Pt^{II}-Cu^{II}-Pt^{II}]\}_n-$ and $[Pt^{II}-Cu^{II}-Pt^{II}]-[Rh_2^{II,II}]-[Pt^{II}-Cu^{II}-Pt^{II}]$, respectively, which are unchanged from those in the starting compounds. However, the charge of the Cu atoms might have fluctuated, because all of the peaks found in **3**−**5** and **7** are closer to that of $Cu^{I}Cl$ (932.2 eV) than to $Cu^{II}Cl_2$ (933.8 eV).[32]

Electronic Structures and Absorption Spectra. The simple molecular orbital diagram of **2**, which represents the interaction between the vacant σ^* orbital of $[Rh_2^{II,II}]$ and the filled d_{z^2} orbital of $[Pt^{II}]_2$, is obtained (Figure 11). The diagram represents the sequence of four molecular orbitals made from all possible combinations of the metal d_{z^2} orbitals. The energy of these molecular orbitals increases with the number of nodes along the chain direction.[33] Taking into account that the dinuclear complexes of $[Rh_2]$ and mononuclear [Pt] in **2** are stacked with staggered forms (Figure 2b), the σ-type orbital is mainly stabilized or destabilized because the overlaps of the π- and δ-type orbitals are less effective, with the result that the vacant σ-type orbitals combined with $d_{z^2}(Pt)-\sigma^*(Rh_2)-d_{z^2}(Pt)$ are destabilized. As shown in Figure S11, the DFT calculation on the model $[\{Rh_2(O_2CCH_3)_4\}\{Pt(NHCOCH_3)_2(NH_3)_2\}_2]$ shows that the LUMO consists of vacant σ-type orbitals $(d_{z^2}(Pt)-\sigma^*(Rh_2)-d_{z^2}(Pt))$ of an antibonding combination of $d_{z^2}(Pt)$ and $\sigma^*(Rh_2)$, and other stabilized σ-type orbitals of HOMO−4 and HOMO−12 are also found. Thus, the validity of the simple schematic molecular orbital diagram in Figure 11 is confirmed by the DFT calculation. The calculation also shows that π-type orbitals in $[Rh_2]$ are also essentially destabilized or stabilized by mixing with the π orbitals of the piam ligands through d_{z^2} in [Pt], showing that the HOMO is π-type orbitals destabilized by the π orbitals of the piam ligands (Figure 11).

Figure 12 shows the diffuse reflectance spectra of **2**−**5**, **7**, and $[Rh_2(O_2CCH_3)_4]$. The spectrum of **2** shows four peaks at 3.45, 2.84 (E_1), 1.74 (E_2), and 1.45 (E_3) eV (Figure 12a) instead of

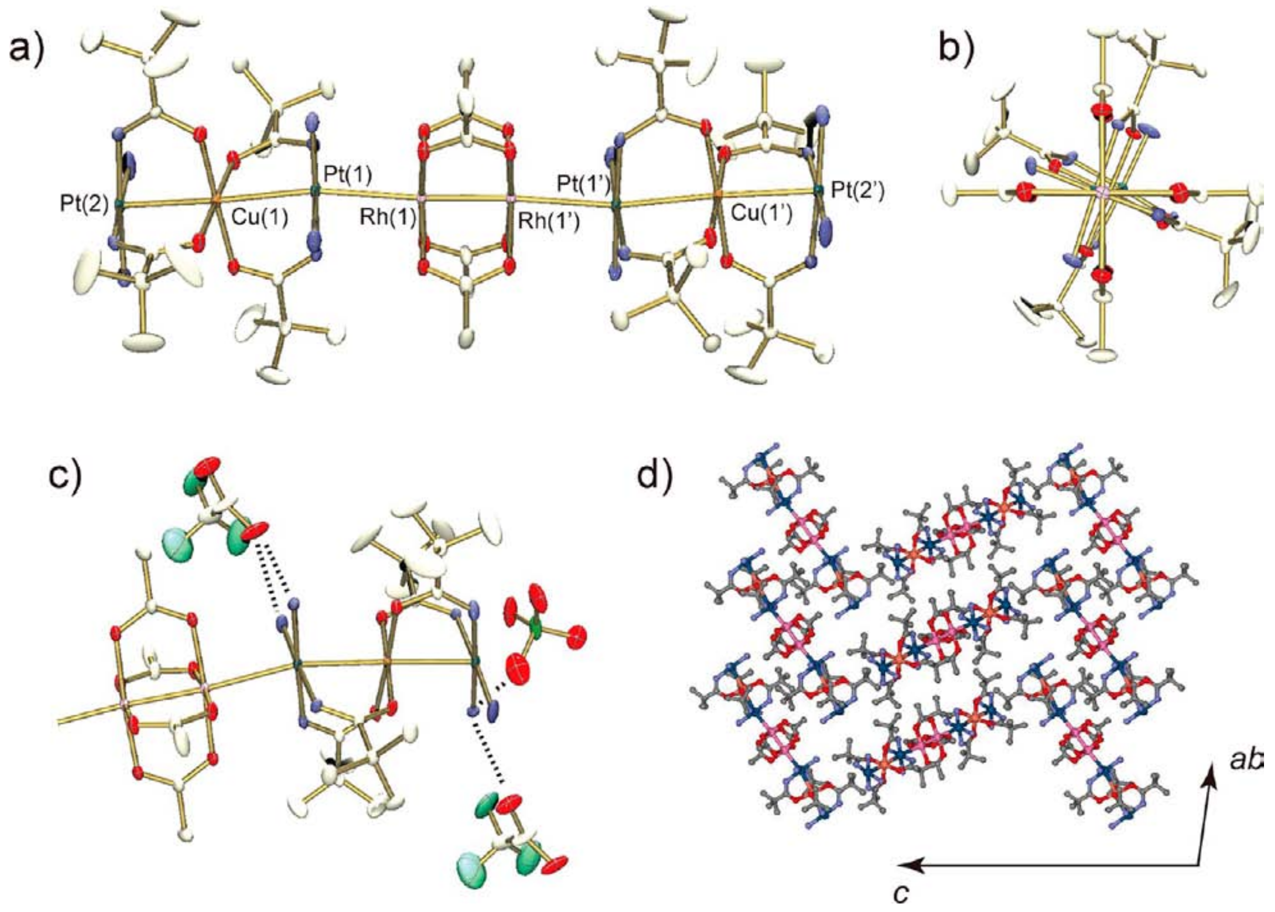

Figure 8. (a) Crystal structure of $[\{Rh_2(O_2CCH_3)_4\}\{Pt_2Cu(piam)_4(NH_3)_4\}_2](CF_3CO_2)_2(ClO_4)_2{\cdot}2H_2O$ (7). (b) View along the metal−metal bond in 7. (c) Hydrogen bonds between the octanuclear complex and $CF_3CO_2^-$ or ClO_4^- ions shown as dotted lines. (d) Crystal packing of the octanuclear complexes in 7. Hydrogen atoms, water molecules, $CF_3CO_2^-$, and ClO_4^- ions are omitted for clarity.

Table 2. Comparison of Metal−Metal Distances (Å) and Selected Angles (deg) between 2−7

compounds	Rh−Rh (Å)	Rh−Pt (Å)	Pt−Cu (Å)	θ_2 (deg)	ϕ_2 (deg)	τ_3 (deg)
2	2.3956(10)[a]	2.8208(8)[a]			29.4[a]	
3			2.6870(6)[a]			16.6[a]
4	2.3701(14)	2.7749(11)	2.7034(9)	155.010(19)	41.2	19.7
5	2.3733(6)	2.7702(4)	2.6716(3)	164.340(7)	34.9	16.8
6	2.3901(7)	2.7954(6)	2.6540(5)	170.711(9)	8.0	14.5
7	2.3826(8)	2.8155(5)	2.7094(6), 2.6560(6)	166.434(19)	19.6	16.4, 15.6

[a] Measured at 293 K.

those around 2.75 and 2.05 eV in $[Rh_2(O_2CCH_3)_4]$, attributed to $\pi^*(Rh_2) \rightarrow \sigma^*(Rh{-}O)$ and $\pi^*(Rh_2) \rightarrow \sigma^*(Rh_2)$ transitions in the Rh_2 core[23] (Figure 12e), and a small peak at 1.90 eV in **3** (Figure 12f). The absorption spectrum obtained from time-dependent (TD) DFT calculations on the singlet state for $[\{Rh_2(O_2CCH_3)_4\}\{Pt(NHCOCH_3)_2(NH_3)_2\}_2]$ shows three characteristic bands at 3.37, 2.62, and 1.76 eV (Table S7 and Figure S13b). The calculated singlet absorption of the three bands (Figure S13b) is due to the transitions from HOMO, HOMO−2, HOMO−4, HOMO−6, or HOMO−7 to the LUMO, whereas HOMO, HOMO−2, HOMO−6, and HOMO−7 are combined orbitals of $\pi^*(Rh_2)$ with d_{z^2}(Pt) (Figure S11). As mentioned above, HOMO−4 consists of stabilized σ-type orbitals, where all orbitals related to absorption bands lie on the metals. Taking into account the large difference between calculated and observed absorption energies, another model of $[\{Rh_2(O_2CCF_3)_4\}\{Pt(NHCOCH_3)_2(NH_3)_2\}_2]$ was studied (Figure S12) and showed a similar absorption profile with three bands at 3.06, 2.11, and 1.71 eV (Table S8 and Figure S13c). The calculated singlet absorptions at 2.11, and 1.71 eV are due to the transitions from HOMO, HOMO−2, HOMO−9, or HOMO−10, which are orbitals with $\pi^*(Rh_2)$ and d_{z^2}(Pt), to the LUMO, which consists of destabilized σ-type orbitals combined with $d_{z^2}(Pt)-\sigma^*(Rh_2)-d_{z^2}(Pt)$ (Figure S12). The calculated singlet absorption at the large peaks of 3.06 eV is due to transitions from HOMO−4, HOMO−6, or HOMO−8, which are stabilized $d_{z^2}(Pt)-\sigma(Rh_2)-d_{z^2}(Pt)$, to the LUMO (Figure S12). Consequently, the larger peak at E_1 is attributed to $d_{z^2}(Pt)-\sigma(Rh_2)-d_{z^2}(Pt) \rightarrow d_{z^2}(Pt)-\sigma^*(Rh_2)-d_{z^2}(Pt)$, while E_2 and E_3 are mixed orbitals with $\pi^*(Rh_2)$ and $d_{z^2}(Pt) \rightarrow d_{z^2}(Pt)-\sigma^*(Rh_2)-d_{z^2}(Pt)$. As mentioned in the previous paragraph, three new peaks at 3.79 (327), 1.90 (651), and around 1.49 eV (830 nm) appear when $[Rh_2(O_2CCH_3)_4]$ and

Scheme 2

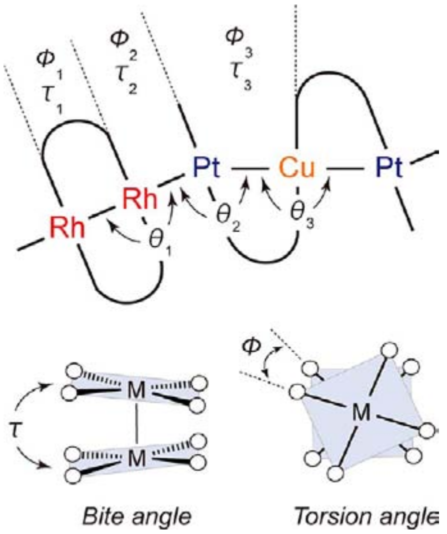

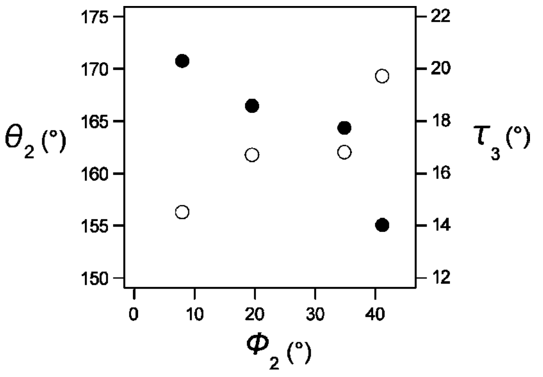

Figure 9. The relationship of θ_2 versus ϕ_2 (filled circles) and τ_3 versus ϕ_2 (open circles).

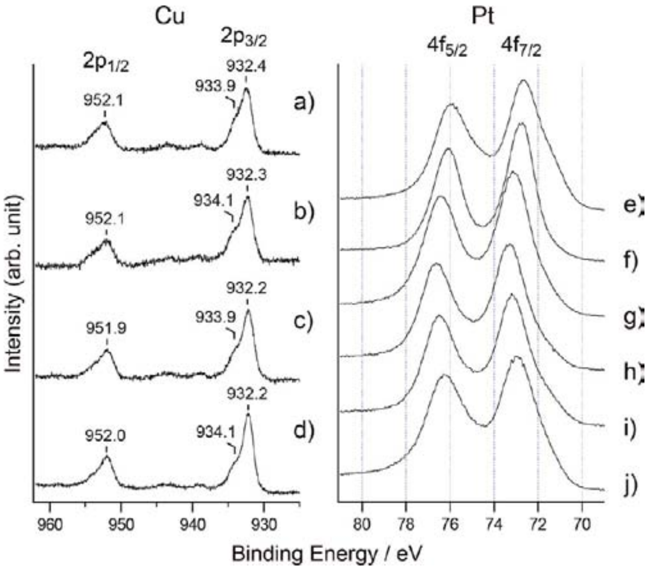

Figure 10. Cu $2p_{1/2}$ and $2p_{3/2}$ (left) core levels of XPS for (a) **3**, (b) **4**, (c) **5**, and (d) **7**. Pt $4f_{5/2}$ and $4f_{7/2}$ (right) core levels of XPS for (e) **1**, (f) **2**, (g) **3**, (h) **4**, (i) **5**, and (j) **7**.

Table 4. The Binding Energies (eV) for 2p Region of Cu, 3d of Rh, and 4f of Pt in 1−5 and 7

	Cu $2p_{1/2}$	Cu $2p_{3/2}$	Rh $3d_{5/2}$	Pt $4f_{5/2}$	Pt $4f_{7/2}$
1				76.0	72.7
2			308.9	76.1	72.7
3	952.1	933.9 (sh), 932.4		76.5	73.2
4	952.1	934.1 (sh), 932.3	308.9	76.6	73.3
5	951.9	933.9 (sh), 932.2	308.7	76.5	73.2
7	952.0	934.1 (sh), 932.2	308.8	76.3	73.0

1 are mixed in THF, the three peaks corresponding to E_1, E_2, and E_3, supporting the fact that these Rh−Pt bonds are also formed in the solution state (Figure S14).

Figure 12b−d show the spectra of **4**, **5**, and **7**. Each spectrum has a similar profile to **2**, having E_1, E_2, and E_3 bands. As summarized in Table 5, these E_2 and E_3 are also observed in compounds discussed earlier,[11d,e] $[\{Rh_2(O_2CCH_3)_4\}\{Pt_2(piam)_2(NH_3)_4\}_2]_n(PF_6)_{4n}\cdot 6nH_2O$, $[\{Rh_2(O_2CCH_3)_4\}\{Pt_2(piam)_2(NH_2CH_3)_4\}_2](PF_6)_4$, and $[\{Rh_2(O_2CCH_3)_4\}\{Pt_2(piam)_2(bpy)_2\}_2](PF_6)_4$, implying characteristic bands found in Rh^{II}−Pt^{II} bond formation. Interestingly, both E_2 and E_3 peaks in **4**, **5**, and **7** are about 0.1 eV lower than those in other compounds, indicating that the HOMO−LUMO gaps are narrower. The reason is probably due to perturbation by the d_{z^2} orbitals of energetically higher Cu ions,[10] and there is

Table 3. Comparison of Rh−Pt Distances (Å) in Reported Compounds and 2−7

compounds[a]	bridged Rh−Pt (Å)	unbridged Rh−Pt (Å)	ref
$[\{PtRh(piam)_2(NH_3)_2Cl_{2.5}\}_2\{Pt_2(piam)_2(NH_3)_4\}_2]_n(PF_6)_{6n}\cdot 2nMeOH\cdot 2nH_2O$	2.5987(11)	2.7337(11)	11a
$[\{PtRh(tcm)_2(NH_3)_2Cl_{2.5}\}_2\{Pt_2(piam)_2(NH_3)_4\}_2]_n(PF_6)_{6n}\cdot 2nH_2O$	2.605(2), 2.602(2)	2.742(2), 2.715(2)	11c
$[PtRh(piam)_2(NH_3)_2Cl_3]\cdot 4H_2O$	2.5704(7)		28
$[PtRh(piam)_2(en)Cl_3]\cdot 3H_2O$	2.5796(19), 2.5771(17)		28
$[\{Rh_2(O_2CCH_3)_4\}\{Pt_2(piam)_2(NH_3)_4\}_2]_n(PF_6)_{4n}\cdot 6nH_2O$		2.7460(10)	11d
$[\{Rh_2(O_2CCF_3)_4\}\{Pt_2(piam)_2(NH_3)_4\}_2]_n(CF_3CO_2)_{4n}\cdot 2nEtOH\cdot 2nH_2O$		2.7473(15)	11d
$[\{Rh_2(acam)_4\}\{Pt_2(piam)_2(NH_3)_4\}_2]_n(CF_3CO_2)_{4n}$		2.7781(14)	11d
$[\{Rh_2(O_2CCH_3)_4\}\{Pt_2(piam)_2(NH_2CH_3)_4\}_2](PF_6)_4$		2.7493(12)	11e
$[\{Rh_2(O_2CCH_3)_4\}\{Pt_2(piam)_2(bpy)_2\}_2](PF_6)_4$		2.7310(5)	11e
2		2.8208(8)[b]	this work
4		2.7749(11)	this work
5		2.7702(4)	this work
6		2.7954(6)	this work
7		2.8155(5)	this work

[a] Abbreviation: tcm = Cl_3CCONH^-, en = ethylenediamine, acam = acetamidate. [b] Measured at 293 K.

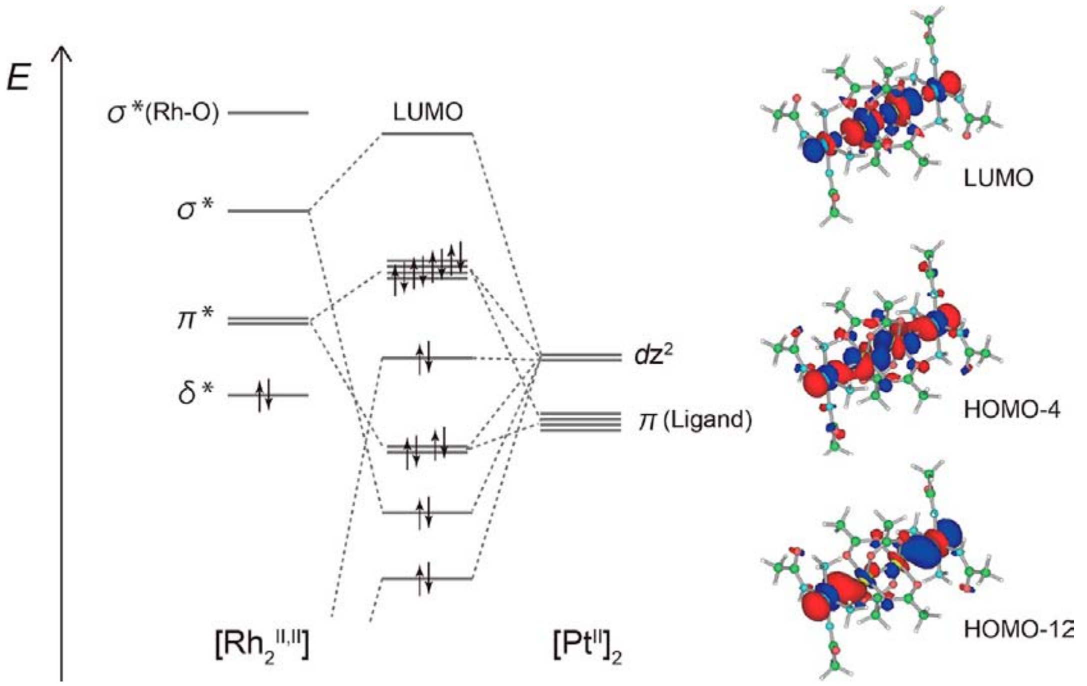

Figure 11. Schematic molecular orbital diagram of **2** with selected molecular orbital shapes in the model of $[\{Rh_2(O_2CCH_3)_4\}\{Pt(NHCOCH_3)_2(NH_3)_2\}_2]$.

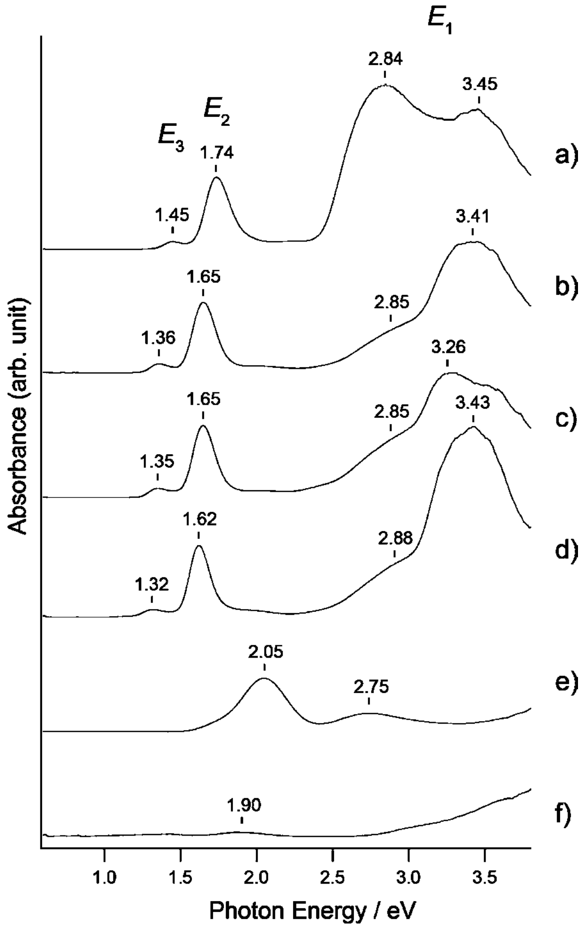

Figure 12. Diffuse reflectance spectra of (a) **2**, (b) **4**, (c) **5**, (d) **7**, (e) $[Rh_2(O_2CCH_3)_4]$, and (f) **3** with MgO at room temperature.

meaningful interaction between Pt and Cu ions, as well as Rh and Pt ions.

EPR Spectra. In **3**–**7**, whether the trinuclear [Pt–Cu–Pt] units are linked to Rh atoms or not, the formal oxidation states of the trinuclear units are $[Pt^{II}–Cu^{II}–Pt^{II}]$, indicating that the unpaired electron lies on the Cu atom. The EPR (X-band) spectra of **3** in MeOH glass and polycrystalline samples of **3**–**7** were measured. The spectrum of **3** in MeOH glass at 77 K shows a well-resolved profile with $g_{\parallel} = 2.351$ and $g_{\perp} = 2.054$ (Figure 13), which is characteristic for Cu $d_{x^2-y^2}$ spin.[8a,d,e,34] These g values are comparable to those in similar trinuclear complexes, *cis*-$[\{Pt(1\text{-}MeU)(1\text{-}MeC)(NH_3)_2\}_2Cu]^{4+}$ (1-MeUH = 1-methyluracil, 1-MeC = 1-methylcytosine, $g_{\parallel}$ = 2.384, $g_{\perp}$ = 2.070) and *cis*-$[\{Pt(1\text{-}MeU)_2(NH_3)_2\}_2Cu]^{2+}$ ($g_{\parallel}$ = 2.367, $g_{\perp}$ = 2.058).[8a] The fact that the $g_{\parallel}$ absorption is at lower field than the $g_{\perp}$ band points to a tetragonal elongation of the ligand field about Cu^{2+}.[8a] Both the $g_{\parallel}$ and $g_{\perp}$ absorptions are split into four components by the Cu nuclear (I = 3/2) hyperfine interaction ($A_{\parallel} = 149 \times 10^{-4}$ cm^{-1} and $A_{\perp} = 18 \times 10^{-4}$ cm^{-1}), accompanied with isotope effects arising from the natural occurrence of ^{63}Cu (I = 3/2, 69.1%) and ^{65}Cu (I = 3/2, 30.9%). As shown in Figure 14a, the spectrum of polycrystalline **3** shows a broad axial-type signal with $g_{\parallel}$ = 2.347 and $g_{\perp}$ = 2.065, where a splitting into four at the $g_{\parallel}$ absorption by the Cu hyperfine interaction ($A_{\parallel} = 147 \times 10^{-4}$ cm^{-1}) was also observed at room temperature.

As shown in Figure 14b–d, the spectra of polycrystalline **4**–**6** at room temperature show axial-type signals with $g_{\parallel} > g_{\perp}$ (Table 6). The electronic structure of **4**–**6** can be validly drawn as the admixture of Cu d orbitals to the schematic molecular orbital diagram of **2** shown in Figure 11, showing that the HOMO (SOMO) is Rh_2 orbitals, destabilized σ-type orbitals, or Cu $d_{x^2-y^2}$ orbitals. Taking into account the relationship between $g_{\perp}$ and $g_{\parallel}$,[9c,11a,35] that is, $\pi^*(Rh_2)$ spin with $g_{\parallel} > 2.0 > g_{\perp}$, $\delta^*(Rh_2)$ spin with $g_{\perp} > 2.0 \approx g_{\parallel}$, and σ-type (Pt or Cu) spin with $g_{\perp} > 2.0 \approx g_{\parallel}$, the observed $g_{\parallel} > g_{\perp} > 2.0$ is evidence that

Table 5. Comparison of E_1, E_2, and E_3 (eV) Found in Reported Compounds, 2, 4, 5, and 7

compounds	E_1 (eV)	E_2 (eV)	E_3 (eV)	ref
$[\{Rh_2(O_2CCH_3)_4\}\{Pt_2(piam)_2(NH_3)_4\}_2]_n(PF_6)_{4n}\cdot 6nH_2O$	3.01, 2.60 (sh)	1.78	1.50	11d
$[\{Rh_2(O_2CCF_3)_4\}\{Pt_2(piam)_2(NH_3)_4\}_2]_n(CF_3CO_2)_{4n}\cdot 2nEtOH\cdot 2nH_2O$	2.67, 2.23 (sh)	1.85	1.55	11d
$[\{Rh_2(O_2CCH_3)_4\}\{Pt_2(piam)_2(NH_2CH_3)_4\}_2](PF_6)_4$	3.05	1.80	1.53	11e
$[\{Rh_2(O_2CCH_3)_4\}\{Pt_2(piam)_2(bpy)_2\}_2](PF_6)_4$	3.21	1.70	1.44	11e
2	3.45, 2.84	1.74	1.45	this work
4	3.41, 2.85 (sh)	1.65	1.36	this work
5	3.26, 2.85 (sh)	1.65	1.35	this work
7	3.43, 2.88 (sh)	1.62	1.32	this work

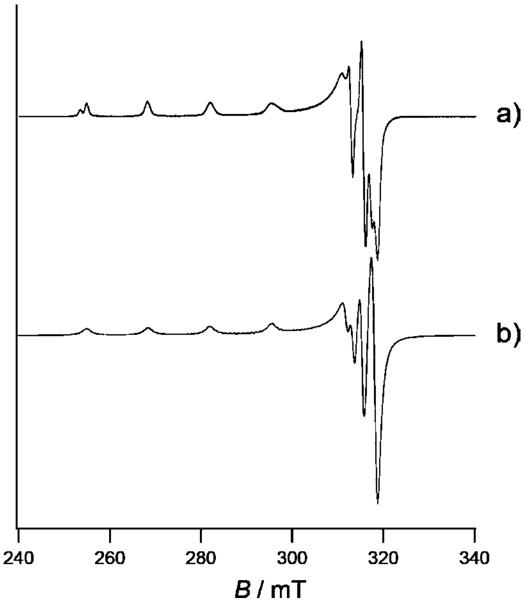

Figure 13. Continuous wave EPR spectra for **3** in MeOH glass at 77 K, (a) observed and (b) simulation. Experimental settings: microwave frequency, 9.05839 GHz; microwave power, 3 mW; field modulation, 0.2 mT.

the unpaired electrons lie in the Cu $d_{x^2-y^2}$ orbitals in **4**–**6**. As shown in Figures S16–S18, the spectra of **4**–**6** were essentially unchanged on cooling to 77 K, showing no change in the local crystal field. At both temperatures, the spectra of **4**–**6** are relatively sharp without hyperfine splitting, which can be explained by an appreciable reduction of the hyperfine coupling constant[8d] or by exchange narrowing.[36] For the former explanation, it is well-known that Cu^{2+} acetylacetonate complexes are axially affected by stronger donor solvents to reduce $A_{||}$ than the isolated compounds with an increase in $g_{||}$ values.[34] If there is an appreciable reduction of $A_{||}$ in **4**–**6** in contrast to the $A_{||}$ values (147×10^{-4} cm^{-1}) of **3**, the Cu hyperfine components for the $g_{||}$ band will be closely overlapped. Among **4**–**6**, the peak widths of $g_{||}$ become sharper as the $g_{||}$ values become larger; however, the $g_{||}$ values of **4**–**6** are smaller than **3**. Thus, the former explanation is not applicable in this case, and the interpretation by exchange narrowing is better. An exchange-coupled pair of Cu^{2+} ions shows that the copper hyperfine structure is smeared out and only a g-anisotropy remains with a Lorentzian line shape,[36] which is characteristic of 1-D structures **4**–**6**. The sharper line shape of **6**, which is induced by the ease of exchange coupling attributed to the straight framework, supports this interpretation.

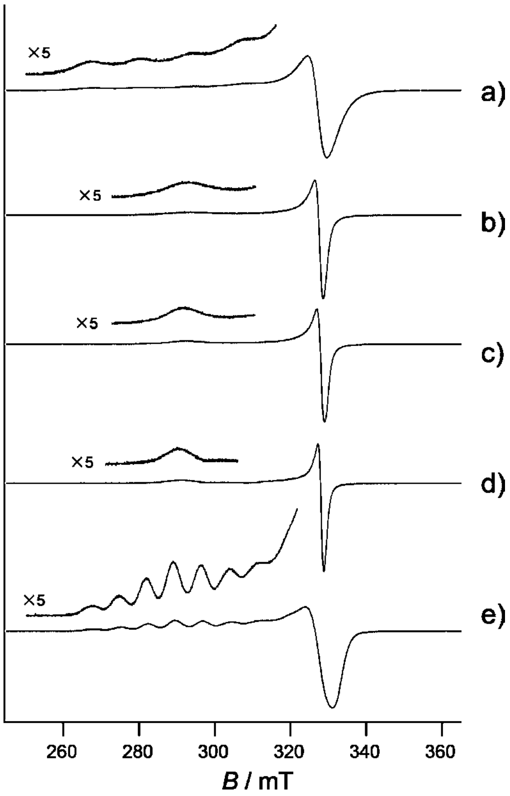

Figure 14. Continuous wave EPR spectra measured at room temperature for powder samples (a) **3**, (b) **4**, (c) **5**, (d) **6**, and (e) **7**. Experimental settings: microwave frequency, 9.4455 (a), 9.4438 (b), 9.4450 (c), 9.4425 (d), and 9.4450 GHz (e); microwave power, 3 mW; field modulation, 0.2 mT.

Table 6. EPR Parameters for Powder Samples 3–7

	room temperature			77 K	
	$g_{||}$	$g_{\perp}$	$A_{||}$ (10^4 cm^{-1})	$g_{||}$	$g_{\perp}$
3	2.347	2.065	147	2.368	2.075
4	2.305	2.061		2.305	2.062
5	2.309	2.059		2.311	2.058
6	2.317	2.057		2.317	2.059
7	2.331	2.060	79	2.319	2.066

As shown in Figure 14e, the spectrum of a polycrystalline **7** is also an axial-type signal with $g_{||} > g_{\perp} > 2.0$ (Table 6), showing that **7** also has an unpaired electron in the Cu $d_{x^2-y^2}$ orbital. Compared with **4**–**6**, the spectrum of **7** is broad, and an unusual seven splittings of the $g_{||}$ absorption with $A_{||} = 79 \times 10^{-4}$ cm^{-1} appeared (Figure 14e). To obtain a well-resolved spectrum, an EPR measurement at 77 K with a single crystal of **7** was carried out. Compound **7** crystallizes with a welldeveloped (011) crystal face, and spectra were measured at 10° intervals for rotations of the (011) plane about the normal to each crystal.[37] Figure 15 shows the spectra from −90° to 90°, where the field vector and (011) plane are parallel at 0°. Although the $g_{\parallel}$ values depend on the angle of the field, obvious seven splittings of the $g_{\parallel}$ absorption are observed at −40°. The 14 splittings at −20° imply that two $g_{\parallel}$ absorptions are closely overlapped because of the two types of orientation of the CuO_4 field in the crystal (Figure 8d). Seven splittings such as these indicate the hyperfine structure corresponding to two equivalents of copper atoms ($I = 3/2$) with rapid spin exchange between the two Cu^{2+} centers (dipole coupling), which is generally observed in compounds having close Cu−Cu distances.[3d,h,8a,36] In such a case, a transition for $\Delta M_s = 1$ around 320 mT with a fine structure arising from large zero-field splitting, and occasionally the forbidden transition at $\Delta M_s = 2$ around 160 mT, was observed. In contrast, in **7**, the closest Cu−Cu distance is 10.2 Å, which is relatively long, and the fine structure as well as the forbidden transition at $\Delta M_s = 2$ was not observed. Therefore, the seven splittings of $g_{\parallel}$ absorption are caused by another mechanism.

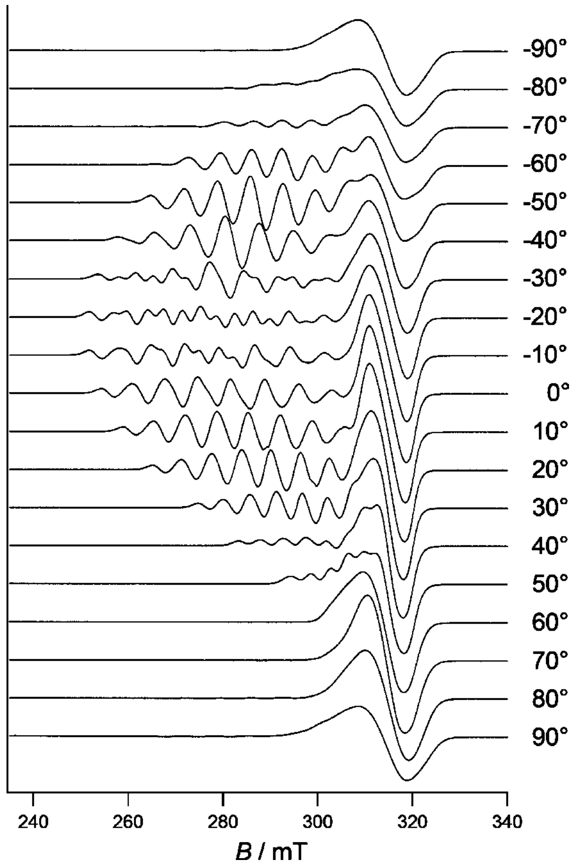

Figure 15. Continuous wave EPR spectra measured at 77 K of **7** for the rotation of the (011) plane in the crystal. Experimental settings: microwave frequency, 9.06 GHz; microwave power, 3 mW; field modulation, 0.2 mT.

Referring to the related Cu^{2+} compounds showing more than four split EPR spectra,[9b,34b,38,39] further splitting originates from (i) the hyperfine coupling by coordinated atoms[9b,38] or (ii) the magnetic dipole coupling between neighboring Cu^{2+} spins.[39] In **7**, because the Cu^{2+} atom is axially sandwiched by two Pt atoms, it is possible to be perturbed by ^{195}Pt ($I = 1/2$, 33.7% natural abundance) atoms, such an interaction being responsible for 1:4:1 splitting. The parallel hyperfine coupling constants of Cu ($= A_{\mathrm{Cu}\parallel}$) observed in related CuO_4 complexes are about 150−200 × 10^{-4} $\mathrm{cm^{-1}}$,[34] whereas, the $A_{\mathrm{Cu}\parallel}$ values of di- or trinuclear copper−platinum complexes containing close Cu^{II}−Pt^{II} distances are 79,[8d] 94,[9c] 121,[8a] and 134 × 10^{-4} $\mathrm{cm^{-1}}$,[8a] with the tendency to decrease. Taking into account that the hyperfine coupling constants of ^{195}Pt are of a similar order (≈ 200 × 10^{-4} $\mathrm{cm^{-1}}$),[11a,40] when the $d_{x^2-y^2}$ spin is interacted with both Cu and ^{195}Pt with the relationship of $2 \times A_{\mathrm{Cu}\parallel} = A_{\mathrm{Pt}\parallel}$, six line spectra with intensity 1:5:6:6:5:1 are expected. Further splitting to seven lines, that is, 1:6:11:12:11:6:1 lines by the overlap of two 1:5:6:6:5:1 lines by the same separation, is attained with the magnetic dipole coupling.[39] It is in fact the magnetic dipole coupling with the unpaired electrons of neighboring paramagnetic centers that causes the relatively broad lines;[36] however, the splittings may sometimes be resolved when the crystal structure of a pure compound is such that each metal has a small number of relatively close paramagnetic neighbors.[39] Scheme 3 shows the schematic view of the crystal structure of **7** with the distances of Cu^{2+}−Cu^{2+}. The closest distance is 10.2 Å between neighboring octanuclear units with the perpendicular orientation relationship, where the magnetic dipole coupling occurs, considering the short distance (2.6560(6) Å) between Cu(1) and Pt(2) in octanuclear **7** (Figure 8a). In practice, the distance between the end Pt and a copper atom in the neighboring unit is 7.6 Å, which is in the possible range of the magnetic dipole coupling.[39c]

Scheme 3

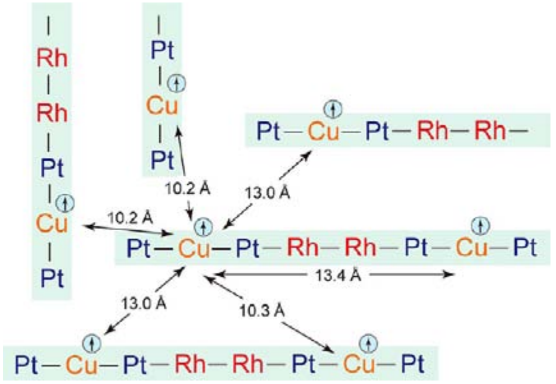

CONCLUSION

This work was devoted to the syntheses and characterization of novel 1-D chains comprised of metal−metal bonds by three metal species, Rh, Pt, and Cu. Taking advantage of unbridged Rh−Pt bonds, we succeeded in obtaining three 1-D chains (**4**−**6**) with the repetition of $-\{[Rh_2]-[Pt-Cu-Pt]\}_n-$, where the angles of Rh−Pt−Cu and stacking fashion between Rh and Pt coordination planes are controlled by the packing effect and accommodated solvent molecules. When the counteranions are $CF_3CO_2^-$ and ClO_4^-, an octameric complex (**7**) with [Pt−Cu−Pt]−[Rh_2]−[Pt−Cu−Pt] alignment was achieved, where each anion obstructs the further extension by hydrogen bonds. The XPS and EPR results showed that the oxidation state of the pentameric unit in **4**−**6** is $-[Rh_2^{II,II}]-[Pt^{II}-Cu^{II}-Pt^{II}]-$, where the HOMO (SOMO) consists of $d_{x^2-y^2}$ of Cu. Also in **7**, each oxidation state is +2; however, the hyperfine coupling in the EPR spectrum indicates that the unpaired spin on Cu is perturbed by Pt atoms. These results imply the possibility of redox between metals and heterometals by 1-D alignment with metal−metal bonds. It is anticipated that such an approach will be applicable in the construction of various novel 1D chains with tailored metal alignments, oxidation states, and electronic structures.

■ ASSOCIATED CONTENT

Ⓢ Supporting Information

Detailed crystal structures, IR spectra, XPS, DFT calculations, EPR spectra with simulation, and crystal information files (CIF) included. This material is available free of charge via the Internet at http://pubs.acs.org.

■ AUTHOR INFORMATION

Corresponding Author

*E-mail: k_uemura@gifu-u.ac.jp.

Notes

The authors declare no competing financial interest.

■ ACKNOWLEDGMENTS

This work was supported by the Grants-in-Aid for Scientific Research (Scientific Research (C) 24550074) and Nippon Sheet Glass Foundation for Materials Science and Engineering. Theoretical calculations were performed using the Research Center for Computational Science, Okazaki, Japan.

■ REFERENCES

(1) (a) Miller, J. S. *Extended Linear Chain Compounds*; Plenum: New York, 1982; Vols *1*−*3*. (b) Kitagawa, H.; Mitani, T. *Coord. Chem. Rev.* **1999**, *190*−*192*, 1169−1184. (c) Bera, J. K.; Dunbar, K. R. *Angew. Chem., Int. Ed.* **2002**, *41*, 4453−4457. (d) Yamashita, M.; Takaishi, S. *Bull. Chem. Soc. Jpn.* **2006**, *79*, 1820−1833. (e) Mashima, K. *Bull. Chem. Soc. Jpn.* **2010**, *83*, 299−312. (f) Givaja, G.; Amo-Ochoa, P.; Gómez-García, C. J.; Zamora, F. *Chem. Soc. Rev.* **2012**, *41*, 115−147.

(2) (a) Tejel, C.; Ciriano, M. A.; Oro, L. A. *Chem.—Eur. J.* **1999**, *5*, 1131−1135. (b) Matsumoto, K.; Sakai, K. *Adv. Inorg. Chem.* **2000**, *49*, 375−427.

(3) For examples of finite 1D metal complexes, see: (a) Lai, S.-Y.; Lin, T.-W.; Chen, Y.-H.; Wang, C.-C.; Lee, G.-H.; Yang, M.-h.; Leung, M.-k.; Peng, S.-M. *J. Am. Chem. Soc.* **1999**, *121*, 250−251. (b) Tejel, C.; Ciriano, M. A.; Villarroya, B. E.; Lopez, J. A.; Lahoz, F. J.; Oro, L. A. *Angew. Chem., Int. Ed.* **2003**, *42*, 529−532. (c) Murahashi, T.; Uemura, T.; Kurosawa, H. *J. Am. Chem. Soc.* **2003**, *125*, 8436−8437. (d) Tanaka, K.; Tengeiji, A.; Kato, T.; Toyama, N.; Shionoya, M. *Science* **2003**, *299*, 1212−1213. (e) Goto, E.; Begum, R. A.; Zhan, S.; Tanase, T.; Tanigaki, K.; Sakai, K. *Angew. Chem., Int. Ed.* **2004**, *43*, 5029−5032. (f) Ruffer, T.; Ohashi, M.; Shima, A.; Mizomoto, H.; Kaneda, Y.; Mashima, K. *J. Am. Chem. Soc.* **2004**, *126*, 12244−12245. (g) Chen, I.-W. P.; Fu, M.-D.; Tseng, W.-H.; Yu, J.-Y.; Wu, S.-H.; Ku, C.-J.; Chen, C.-h.; Peng, S.-M. *Angew. Chem., Int. Ed.* **2006**, *45*, 5814−5818. (h) Liu, I. P.-C.; Lee, G.-H.; Peng, S.-M.; Bénard, M.; Rohmer, M.-M. *Inorg. Chem.* **2007**, *46*, 9602−9608.

(4) For recent reports on infinite 1D chains, see: (a) Finniss, G. M.; Canadell, E.; Campana, C.; Dunbar, K. R. *Angew. Chem., Int. Ed.* **1996**, *35*, 2772−2774. (b) Prater, M. E.; Pence, L. E.; Clerac, R.; Finniss, G. M.; Campana, C.; Auban-Senzier, P.; Jerome, D.; Canadell, E.; Dunbar, K. R. *J. Am. Chem. Soc.* **1999**, *121*, 8005−8016. (c) Cotton, F. A.; Dikarev, E. V.; Petrukhina, M. A. *J. Chem. Soc., Dalton Trans.* **2000**, 4241−4243. (d) Pruchnik, F. P.; Jakimowicz, P.; Ciunik, Z.; Stanislawek, K.; Oro, L. A.; Tejel, C.; Ciriano, M. A. *Inorg. Chem. Commun.* **2001**, *4*, 19−22. (e) Sakai, K.; Ishigami, E.; Konno, Y.; Kajiwara, T.; Ito, T. *J. Am. Chem. Soc.* **2002**, *124*, 12088−12089. (f) Mitsumi, M.; Goto, H.; Umebayashi, S.; Ozawa, Y.; Kobayashi, M.; Yokoyama, T.; Tanaka, H.; Kuroda, S.-i.; Toriumi, K. *Angew. Chem., Int. Ed.* **2005**, *44*, 4164−4168. (g) Mitsumi, M.; Ueda, H.; Furukawa, K.; Ozawa, Y.; Toriumi, K.; Kurmoo, M. *J. Am. Chem. Soc.* **2008**, *130*, 14102−14104. (h) Guijarro, A.; Castillo, O.; Calzolari, A.; Miguel, P. J. S.; Gómez-García, C. J.; Felice, R. d.; Zamora, F. *Inorg. Chem.* **2008**, *47*, 9736−9738. (i) Campbell, M. G.; Powers, D. C.; Raynaud, J.; Graham, M. J.; Xie, P.; Lee, E.; Ritter, T. *Nature Chem.* **2011**, *3*, 949−953.

(5) For recent reports on halogen-bridged infinite 1D chains, see: (a) Kitagawa, H.; Onodera, N.; Sonoyama, T.; Yamamoto, M.; Fukawa, T.; Mitani, T.; Seto, M.; Maeda, Y. *J. Am. Chem. Soc.* **1999**, *121*, 10068−10080. (b) Mitsumi, M.; Murase, T.; Kishida, H.; Yoshinari, T.; Ozawa, Y.; Toriumi, K.; Sonoyama, T.; Kitagawa, H.; Mitani, T. *J. Am. Chem. Soc.* **2001**, *123*, 11179−11192. (c) Yamashita, M.; Kawakami, D.; Matsunaga, S.; Nakayama, Y.; Sasaki, M.; Takaishi, S.; Iwahori, F.; Miyasaka, H.; Sugiura, K.; Wada, Y.; Miyamae, H.; Matsuzaki, H.; Okamoto, H.; Tanaka, H.; Marumoto, K.; Kuroda, S. *Angew. Chem., Int. Ed.* **2004**, *43*, 4763−4767. (d) Takaishi, S.; Kawakami, D.; Yamashita, M.; Sasaki, M.; Kajiwara, T.; Miyasaka, H.; Sugiura, K.-i.; Wakabayashi, Y.; Sawa, H.; Matsuzaki, H.; Kishida, H.; Okamoto, H.; Watanabe, H.; Tanaka, H.; Marumoto, K.; Ito, H.; Kuroda, S.-i. *J. Am. Chem. Soc.* **2006**, *128*, 6420−6425. (e) Kobayashi, A.; Kojima, T.; Ikeda, R.; Kitagawa, H. *Inorg. Chem.* **2006**, *45*, 322−327. (f) Mitsumi, M.; Yoshida, Y.; Kohyama, A.; Kitagawa, Y.; Ozawa, Y.; Kobayashi, M.; Toriumi, K.; Tadokoro, M.; Ikeda, N.; Okumura, M.; Kurmoo, M. *Inorg. Chem.* **2009**, *48*, 6680−6691.

(6) (a) Usón, R.; Foniés, J.; Tomás, M.; Casas, J. M. *J. Am. Chem. Soc.* **1985**, *107*, 2556−2557. (b) Cotton, F. A.; Poli, R. *Inorg. Chem.* **1987**, *26*, 590−595. (c) Cotton, F. A.; Falvello, L. R.; Usón, R.; Fornies, J.; Tomas, M.; Casas, J. M.; Ara, I. *Inorg. Chem.* **1987**, *26*, 1366−1370. (d) Usón, R.; Forniés, J.; Espinet, P.; Fortuño, C.; Tomas, M. *J. Chem. Soc., Dalton Trans.* **1988**, 3005−3009. (e) Balch, A. L.; Rowley, S. P. *J. Am. Chem. Soc.* **1990**, *112*, 6139−6140. (f) Krumm, M.; Lippert, B.; Randaccio, L.; Zangrando, E. *J. Am. Chem. Soc.* **1991**, *113*, 5129−5130. (g) Yamaguchi, T.; Yamazaki, F.; Ito, T. *J. Am. Chem. Soc.* **2001**, *123*, 743−744. (h) Moret, M.-E.; Chen, P. *J. Am. Chem. Soc.* **2009**, *131*, 5675−5690.

(7) Zangrando, E.; Pichierri, F.; Randaccio, L.; Lippert, B. *Coord. Chem. Rev.* **1996**, *156*, 275−332.

(8) For an example of [Pt−Cu−Pt] complexes, see: (a) Lippert, B.; Thewalt, U.; Schöllhorn, H.; Goodgame, D. M. L.; Rollins, R. W. *Inorg. Chem.* **1984**, *23*, 2807−2813. (b) Mutikainen, I.; Orama, O.; Pajunen, A. *Inorg. Chim. Acta* **1987**, *137*, 189−193. (c) Frommer, G.; Lianza, F.; Albinati, A.; Lippert, B. *Inorg. Chem.* **1992**, *31*, 2434−2439. (d) Schreiber, A.; Krizanovic, O.; Fusch, E. C.; Lippert, B.; Lianza, F.; Albinati, A.; Hill, S.; Goodgame, D. M. L.; Stratemeier, H.; Hitchman, M. A. *Inorg. Chem.* **1994**, *33*, 6101−6110. (e) Erxleben, A.; Albinati, A.; Lippert, B. *J. Chem. Soc., Dalton Trans.* **1996**, 1823−1828. (f) Chen, W.; Matsumoto, K. *Eur. J. Inorg. Chem.* **2002**, 2664−2670. (g) Chen, W.; Liu, F.; Nishioka, T.; Matsumoto, K. *Eur. J. Inorg. Chem.* **2003**, 4234−4243. (h) Chen, C.; Qiu, H.; Liu, F.; Chen, W. *J. Chem. Crystallogr.* **2007**, *37*, 619−622. (i) Moret, M.-E.; Chen, P. *Eur. J. Inorg. Chem.* **2010**, 438−446.

(9) For an example of [Pt−Cu] complexes, see: (a) Neugebauer, D.; Lippert, B. *J. Am. Chem. Soc.* **1982**, *104*, 6596−6601. (b) Fusch, G.; Fusch, E. C.; Erxleben, A.; Hüttermann, J.; Scholl, H.-J.; Lippert, B. *Inorg. Chim. Acta* **1996**, *252*, 167−178. (c) Ichieda, N.; Kamimura, T.; Wasada-Tsutsui, Y.; Funahashi, Y.; Ozawa, T.; Jitsukawa, K.; Masuda, H. *Chem. Lett.* **2008**, *37*, 1220−1221.

(10) Goodgame, D. M. L.; Hitchman, M. A.; Lippert, B. *Inorg. Chem.* **1986**, *25*, 2191−2194.

(11) (a) Uemura, K.; Fukui, K.; Nishikawa, H.; Arai, S.; Matsumoto, K.; Oshio, H. *Angew. Chem., Int. Ed.* **2005**, *44*, 5459−5464. (b) Uemura, K.; Fukui, K.; Yamasaki, K.; Matsumoto, K. *Sci. Technol. Adv. Mater.* **2006**, *7*, 461−467. (c) Uemura, K.; Fukui, K.; Yamasaki, K.; Matsumoto, K.; Ebihara, M. *Inorg. Chem.* **2010**, *49*, 7323−7330. (d) Uemura, K.; Ebihara, M. *Inorg. Chem.* **2011**, *50*, 7919−7921. (e) Uemura, K.; Sakurai, K.; Yasuda, E.; Ebihara, M. *Polyhedron* **2012**, *45*, 35−42.

(12) Chen, W.; Matsumoto, K. *Inorg. Chim. Acta* **2003**, *342*, 88−96.

(13) Rempel, G. A.; Legzdins, P.; Smith, H.; Wilkinson, G. *Inorg. Syn.* **1972**, *13*, 90−91.

(14) *REQAB*, version 1.1; Rigaku Corporation: Tokyo, Japan, 1998.

(15) Altomare, A.; Burla, M. C.; Camalli, M.; Cascarano, G. L.; Giacovazzo, C.; Guagliardi, A.; Moliterni, A. G. G.; Polidori, G.; Spagna, R. *J. Appl. Crystallogr.* **1999**, *32*, 115−119.

(16) Sheldrick, G. M. *Acta Crystallogr.* **2008**, *A64*, 112−122.

(17) Yadokari-XG, Software for Crystal Structure Analyses, Wakita K. 2001; Release of Software (Yadokari-XG 2009) for Crystal Structure Analyses: Kabuto, C.; Akine, S.; Nemoto, T.; Kwon, E. *J. Cryst. Soc. Jpn.* **2009**, *51*, 218−224.

(18) (a) Becke, A. D. *J. Chem. Phys.* **1993**, *98*, 5648−5652. (b) Miehlich, B.; Savin, A.; Stoll, H.; Preuss, H. *Chem. Phys. Lett.* **1989**, *157*, 200−206. (c) Lee, C. T.; Yang, W. T.; Parr, R. G. *Phys. Rev. B* **1988**, *37*, 785−789.

(19) Frisch, M. J.; Trucks, G. W.; Schlegel, H. B.; Scuseria, G. E.; Robb, M. A.; Cheeseman, J. R.; Scalmani, G.; Barone, V.; Mennucci, B.; Petersson, G. A.; Nakatsuji, H.; Caricato, M.; Li, X.; Hratchian, H. P.; Izmaylov, A. F.; Bloino, J.; Zheng, G.; Sonnenberg, J. L.; Hada, M.; Ehara, M.; Toyota, K.; Fukuda, R.; Hasegawa, J.; Ishida, M.; Nakajima, T.; Honda, Y.; Kitao, O.; Nakai, H.; Vreven, T.; Montgomery, J. A., Jr.; Peralta, J. E.; Ogliaro, F.; Bearpark, M.; Heyd, J. J.; Brothers, E.; Kudin, K. N.; Staroverov, V. N.; Keith, T.; Kobayashi, R.; Normand, J.; Raghavachari, K.; Rendell, A.; Burant, J. C.; Iyengar, S. S.; Tomasi, J.; Cossi, M.; Rega, N.; Millam, J. M.; Klene, M.; Knox, J. E.; Cross, J. B.; Bakken, V.; Adamo, C.; Jaramillo, J.; Gomperts, R.; Stratmann, R. E.; Yazyev, O.; Austin, A. J.; Cammi, R.; Pomelli, C.; Ochterski, J. W.; Martin, R. L.; Morokuma, K.; Zakrzewski, V. G.; Voth, G. A.; Salvador, P.; Dannenberg, J. J.; Dapprich, S.; Daniels, A. D.; Farkas, O.; Foresman, J. B.; Ortiz, J. V.; Cioslowski, J.; Fox, D. J. *Gaussian 09*, revision C.01; Gaussian, Inc.: Wallingford, CT, 2010.

(20) Hay, P. J.; Wadt, W. R. *J. Chem. Phys.* **1985**, *82*, 299−310.

(21) Hariharan, P. C.; Pople, J. A. *Theor. Chim. Acta* **1973**, *28*, 213−222.

(22) (a) Casida, M. E.; Jamorski, C.; Casida, K. C.; Salahub, D. R. *J. Chem. Phys.* **1998**, *108*, 4439−4449. (b) Stratmann, R. E.; Scuseria, G. E.; Frisch, M. J. *J. Chem. Phys.* **1998**, *109*, 8218−8224.

(23) Cotton, F. A.; Murillo, C. A.; Walton, R. A. *Multiple Bonds Between Metal Atoms*, 3rd ed.; Springer Science and Business Media, Inc.: New York, 2005.

(24) Matsumoto, K.; Sakai, K. *Adv. Inorg. Chem.* **2000**, *49*, 375−427.

(25) (a) Erxleben, A.; Lippert, B. *J. Chem. Soc., Dalton Trans.* **1996**, 2329−2333. (b) Chen, W.; Liu, F.; Matsumoto, K.; Autschbach, J.; Guennic, B. L.; Ziegler, T.; Maliarik, M.; Glaser, J. *Inorg. Chem.* **2006**, *45*, 4526−4536. (c) Chen, W.; Liu, F.; Xu, D.; Matsumoto, K.; Kishi, S.; Kato, M. *Inorg. Chem.* **2006**, *45*, 5552−5560. (d) Hayoun, R.; Zhong, D. K.; Rheingold, A. L.; Doerrer, L. H. *Inorg. Chem.* **2006**, *45*, 6120−6122. (e) Givaja, G.; Castillo, O.; Mateo, E.; Gallego, A.; Gómez-García, C. J.; Calzolari, A.; Felice, R. d.; Zamora, F. *Chem.—Eur. J.* **2012**, *18*, 15476−15484.

(26) Doerrer, L. H. *Dalton Trans.* **2010**, *39*, 3543−3553.

(27) Cotton, F. A.; DeBoer, B. G.; LaPrade, M. D.; Pipal, J. R.; Ucko, D. A. *Acta Crystallogr.* **1971**, *B27*, 1664.

(28) Uemura, K.; Yamasaki, K.; Fukui, K.; Matsumoto, K. *Eur. J. Inorg. Chem.* **2007**, 809−815.

(29) Nag, S.; Banerjee, K.; Datta, D. *New J. Chem.* **2007**, *31*, 832−834.

(30) Nefedov, V. I.; Salyn, Y. V.; Labutin, V. Y.; Baranovskii, I. B. *Koord. Khim.* **1987**, *13*, 103−105.

(31) Matsumoto, K.; Sakai, K.; Nishio, K.; Tokisue, Y.; Ito, R.; Nishide, T.; Shichi, Y. *J. Am. Chem. Soc.* **1992**, *114*, 8110−8118.

(32) Klein, J. C.; Proctor, A.; Hercules, D. M.; Black, J. F. *Anal. Chem.* **1983**, *55*, 2055−2059.

(33) Villarroya, B. E.; Tejel, C.; Rohmer, M.-M.; Oro, L. A.; Ciriano, M. A.; Bénard, M. *Inorg. Chem.* **2005**, *44*, 6536−6544.

(34) (a) Yokoi, H.; Isobe, T. *Bull. Chem. Soc. Jpn.* **1966**, *39*, 2054. (b) Antosik, S.; Brown, N. M. D.; McConnell, A. A.; Porte, A. L. *J. Chem. Soc. A* **1969**, 545−550. (c) Adato, I.; Eliezer, I. *J. Chem. Phys.* **1971**, *54*, 1472−1476. (d) Yokoi, H.; Kishi, T. *Chem. Lett.* **1973**, 749−754.

(35) Kawamura, T.; Katayama, H.; Nishikawa, H.; Yamabe, T. *J. Am. Chem. Soc.* **1989**, *111*, 8156−8160.

(36) Abragam, A.; Bleaney, B. *Electron Paramagnetic Resonance of Transition Ions*; Dover Publication, Inc.: New York, 1986.

(37) Because octanuclear complexes of 7 are perpendicular to one another and packed with a tilt to the (011) plane in the crystal, it is difficult to measure spectra following the Cu crystal field.

(38) Leh, F.; Chan, K. M. *Bull. Chem. Soc. Jpn.* **1972**, *45*, 2709−2711.

(39) (a) Hitchman, M. A. *J. Chem. Phys.* **1978**, *68*, 3425−3432. (b) So, H.; G. P. Haight, J.; Belford, R. L. *J. Phys. Chem.* **1980**, *84*, 1849−1852. (c) Evenhuis, C. J.; Hitchman, M. A.; McDonald, R. G.; Goodgame, D. M. L.; Kwiatkowski, E.; Dettlaff-Weglikowska, U.; Pakawatchai, C.; White, A. H. *J. Chem. Soc., Dalton Trans.* **1984**, 943−952.

(40) Arrizabalaga, P.; Castan, P.; Geoffroy, M.; Laurent, J.-P. *Inorg. Chem.* **1985**, *24*, 3656−3660.